Commun Nonlinear Sci Numer Simulat 134 (2024) 107994

Contents lists available at ScienceDirect

Communications in Nonlinear Science and Numerical Simulation

journal homepage: www.elsevier.com/locate/cnsns

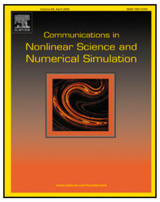

Research paper

Global sensitivity analysis of plasma instabilities via active subspaces

Soraya Terrab[1], Stephen Pankavich *,[1]

Department of Applied Mathematics and Statistics, Colorado School of Mines, Golden, CO 80401, USA

ARTICLE INFO

Keywords:
Vlasov–Poisson
Instability
Active subspace

ABSTRACT

Active subspace analysis is a useful computational tool to identify and exploit the most important linear combinations in the space of a model's input parameters. These directions depend inherently on a quantity of interest, which can be represented as a function from input parameters to model outputs. As the dynamics of many plasma models are driven by potentially uncertain parameter values, the utilization of active subspaces to perform global sensitivity analysis represents an important step in understanding how certain physical phenomena depend upon fluctuations in the values of these parameters. In the current paper, we construct and implement new computational methods to quantify the induced uncertainty within the growth rate generated by perturbations in a collisionless plasma modeled by the one-dimensional Vlasov–Poisson system near an unstable, spatially-homogeneous steady state in the linear regime.

1. Introduction

A number of plasma models require the strict knowledge of input parameters in order to tune them to experimental studies or validate computational simulations. For example, scientists studying Landau damping [1–4], i.e. the stability and exponential decay of a collective mode of oscillations in a plasma without the consideration of collisions among charged particles, must first identify the parameter regimes within which such behavior occurs in order to understand the inherent structure of solutions. Another phenomenon of extreme interest within the plasma physics community is the study of plasma instabilities, such as the Two-Stream and Bump-on-Tail instabilities, which arise from perturbations in the particle distribution function near an unstable, double-humped steady state distribution. These instabilities play a significant role in the theoretical study of plasmas and can be applied to better understand the properties of charged beams in particle accelerators and magnetic confinement devices [5,6].

While prior studies focus on theoretical results concerning the behavior of a deterministic model for electrostatic plasma interactions, in reality, the physical system depends inherently upon knowledge of a variety of parameters, which are often themselves influenced or determined by experimental data. As such information may possess intrinsic uncertainty due to measurement errors, it is crucial to understand how this level of uncertainty can propagate within the output variables of the model. In the context of plasma instabilities, tools from the fields of uncertainty quantification [7,8] and computational science [9] can allow scientists and engineers to make predictions regarding the influence of model parameters. Hence, it is the central purpose of this article to quantify the uncertainty within the growth rate from an unstable steady state that is created by random fluctuations in model parameters, including the mean drift velocity and thermal velocity of the state (henceforth denoted by μ and σ^2, respectively) and the amplitude and frequency of associated oscillations (i.e. α and k herein).

---

* Corresponding author.
E-mail addresses: sterrab@mines.edu (S. Terrab), pankavic@mines.edu (S. Pankavich).

[1] The authors were supported by National Science Foundation, USA grants DMS-1551229, DMS-1614586, and DMS-2107938.

https://doi.org/10.1016/j.cnsns.2024.107994
Received 4 September 2023; Received in revised form 12 March 2024; Accepted 19 March 2024

2. Plasma instabilities

It is well known that collisionless plasmas can experience instabilities generated by perturbations from an associated steady state. For instance, such instabilities are known to occur in particle beams, i.e. accelerated streams of charged particles (ions and electrons). In the laboratory, these beams are created by particle accelerators, like cathode ray tubes and cyclotrons, while such phenomena are naturally created by strong electric fields, as occur in double layers. Particle beams possess a wide range of applications to Inertial Confinement Fusion (ICF) [10,11], fast ignition fusion [12], astrophysics [13,14], and high energy density physics [15], among many others. Here, the background plasma presents a means of current and charge neutralization for charged particle beams, enabling the ballistic propagation of an intense beam pulse [16]. However, the beam streaming through the background plasma can lead to the development of many different instabilities, including the Bump-on-Tail and Two-Stream instabilities, which we will investigate below.

In order to capture this unstable behavior for an electrostatic plasma, we will utilize illustrative examples arising from the Vlasov–Poisson system posed in a spatially-periodic two-dimensional phase space (x, v) with $0 \leq x \leq L$, $-\infty < v < \infty$, and $t \geq 0$ representing time. In dimensionless form, this model is given by

$$\partial_t f + v\partial_x f - E\partial_v f = 0 \tag{1a}$$

$$\partial_x E = 1 - \int f(t,x,v)\, dv. \tag{1b}$$

Here, $f(t,x,v)$ represents the electron distribution function with a fixed and normalized ionic background density, and $E(t,x)$ is the electric field induced by the charges in the system. This system of partial differential equations is obtained by reducing the dimension of the parameter space in the original (dimensional) model via rescaling (Appendix A).

In the case of linearized instability, i.e. the study of the Vlasov–Poisson system linearized about a spatially-homogeneous state $f_{eq}(v)$, precise analytic results regarding the growth rate have been established [17–19]. Here, one assumes the perturbative solution

$$f(t,x,v) = f_{eq}(v) + \delta f(t,x,v)$$

where the perturbation satisfies the plane wave form

$$\begin{aligned} \delta f(t,x,v) &= \alpha f_1(v)\exp(i[kx - \omega t]) \\ E(t,x) &= E_1 \exp(i[kx - \omega t]), \end{aligned}$$

while ignoring the contribution from the resulting nonlinear term in the Vlasov equation. In particular, for sufficiently small α with $0 < \alpha \ll 1$, the associated electric field may grow or decay exponentially in the time-asymptotic limit, and the corresponding rate γ can be completely determined for a given perturbation frequency k. More specifically, if we decompose the temporal frequency into its real and imaginary components

$$\omega(k) = \omega_R(k) + i\gamma(k),$$

where both ω_R and γ are real-valued, then the induced electric field $E(t,x;k)$ grows or decays exponentially with rate $\gamma(k)$ and oscillates at a frequency $\omega_R(k)$ where these values can be determined as roots of the dielectric function [17,20]

$$\varepsilon(k,\omega) = 1 - \frac{1}{k^2}\int \frac{f'_{eq}(v)}{v - \omega/k}\, dv. \tag{2}$$

The relation $\varepsilon(k,\omega) = 0$ is then called the dispersion relation corresponding to the steady state $f_{eq}(v)$. This quantity dictates the existence of so-called normal modes of the system and provides a relationship between the wavenumber and frequency of a perturbation wave, while describing the conditions under which the wave will or will not propagate. Namely, for a given wavenumber k, we define $\gamma(k) = \mathrm{Im}(\omega(k))$ where $\varepsilon(k,\omega(k)) = 0$. The corresponding steady state is deemed (linearly) stable under suitably small perturbations of wavenumber k for $\gamma(k) < 0$, as the perturbed electric field decays to zero exponentially fast, and unstable for $\gamma(k) > 0$, as the resulting field amplitude grows exponentially in time. While the roots of (2) are independent of the perturbation amplitude α, this value must be sufficiently small to guarantee the validity of the perturbative regime. Additionally, we note that the dispersion relation only strictly applies to solutions for which $\gamma(k) > 0$ or $\gamma(k) < 0$, as the dielectric function $\varepsilon(k,\omega)$ suffers a discontinuity along the curve $\gamma = 0$. Furthermore, for $\gamma(k) < 0$ initial wave-like perturbations may not give rise to an electric field with only linear exponential behavior in time. For instance, solutions that demonstrate Gaussian-like behavior in time can be constructed, though these are ultimately dominated by linear exponential decay as t grows large [21]. These ideas have served as a point of contention and confusion since Landau's [1] original work, which analytically continued (2) into the complex plane for $\gamma < 0$ even though the dielectric function fails to remain analytic along $\gamma = 0$, ultimately arriving at solutions that, strictly speaking, are not normal modes of the system. Such issues were originally clarified by van Kampen [22] and Case [23], but have been refined more recently using Cauchy-type integrals by Lee and Shadwick [21], which also resolved inconsistencies between these approaches and Jackson's [24] expansion of Landau's study. More generally this analysis can be extended beyond plane wave solutions and made more precise for general initial data using the Laplace (in t) and Fourier (in x) transforms to solve the linearized Vlasov–Poisson system, as the form of the solution will depend upon all modes, rather than a single wave (see [21]).

In the current context, we will be concerned with parameter regimes in which the values of γ may be positive, leading to the development of instabilities, but can be possibly reduced in magnitude due to variations in parameters related to the physical properties of the steady state. To be clear, the steady state distributions we consider may give rise to both stable and unstable behavior for differing parameter values, and we seek to identify parameter regimes in which the unstable response to the perturbation wave can be tamed. More specifically, we will consider two specific states – the so-called Two-Stream distribution and the Bi-Maxwellian (sometimes referred to as the "double Maxwellian") distribution – in order to perform numerical studies of the growth rate of perturbative solutions. The Two-Stream distribution with mean drift velocity $\mu \in \mathbb{R}$ and scale parameter $\sigma^2 > 0$ is given by the formula

$$f_{TS}(v;\mu,\sigma^2) = \frac{1}{\sqrt{2\pi\sigma^2}} \frac{|v-\mu|^2}{\sigma^2} \exp\left(-\frac{1}{2\sigma^2}|v-\mu|^2\right).$$

We note that the scale parameter is directly obtained from the average thermal velocity via the relationship $v_{\rm th} = \sqrt{3}\sigma$. Hence, using the original dimensional variables the scale parameter σ^2 can be specifically represented as a constant multiple of $k_B T/m$ where m is a particle mass, T is temperature, and k_B is the Boltzmann constant (Appendix A).

After a few standard calculations (see Appendix B), one computes a more precise representation for the dispersion relation, namely

$$\varepsilon_{TS}(k,\omega) = 1 - \frac{1}{\sigma^2 k^2}\left[1 - 2A(u)^2 + 2\left(A(u) - A(u)^3\right) Z(A(u))\right] \tag{3}$$

where we have denoted the phase velocity by $u = \omega/k$, the function

$$A(u) = \frac{1}{\sqrt{2\sigma^2}}(u-\mu),$$

and $Z(\cdot)$ to be the plasma Z-function, given by

$$Z(z) = \frac{1}{\sqrt{\pi}} \int_{-\infty}^{\infty} \frac{e^{-t^2}}{t-z}\, dt \tag{4}$$

for any complex z. Similar to analytic results concerning the Landau damping [1,25] of perturbations from the Maxwellian equilibrium, the exact roots of the dispersion function for the Two-Stream instability cannot be precisely obtained via analytic means and must be either estimated or computationally approximated in order to generate the corresponding rate $\gamma_{TS}(k,\mu,\sigma^2)$.

We will also study the behavior near a different state with similarly-defined parameters, namely the Bi-Maxwellian function given by

$$f_{BM}(v;\mu_1,\mu_2,\sigma_1^2,\sigma_2^2,\beta) = \frac{\beta}{\sqrt{2\pi\sigma_1^2}} \exp\left(-\frac{1}{2\sigma_1^2}|v-\mu_1|^2\right) + \frac{1-\beta}{\sqrt{2\pi\sigma_2^2}} \exp\left(-\frac{1}{2\sigma_2^2}|v-\mu_2|^2\right),$$

along with the constraint $0 < \beta < 1$. Here, the steady state distribution is merely a convex combination of two Maxwellians, and the parameters μ_1, μ_2 and σ_1^2, σ_2^2 again represent the mean drift velocity and average thermal velocity of each separate Maxwellian, respectively, while the parameter β controls the relative densities of the Maxwellians contributing to the velocity distribution. In this case, the dispersion relation can be analogously simplified (Appendix B) to arrive at

$$\varepsilon_{BM}(k,\omega) = 1 + \frac{\beta}{\sigma_1^2 k^2}\left[1 + A_1(u) Z(A_1(u))\right] + \frac{1-\beta}{\sigma_2^2 k^2}\left[1 + A_2(u) Z(A_2(u))\right], \tag{5}$$

where u and Z are defined as before and

$$A_i(u) = \frac{1}{\sqrt{2\sigma_i^2}}\left(u - \mu_i\right)$$

for $i = 1, 2$. As for the Two-Stream distribution, the zeros of the dispersion function cannot be analytically computed, and an analytic approximation will not yield precise roots. Instead, a computational approach is needed to determine the influence of parameter variations on the associated rate of instability, in this case given by $\gamma_{BM}(k,\mu_1,\mu_2,\sigma_1^2,\sigma_2^2,\beta)$. Thus, we will perform a global sensitivity analysis via active subspace methods described in the following section to investigate the relationship between the growth rate of the instability and specific parameters in the system.

3. Active subspaces and global sensitivity analysis

Modern simulations of plasma dynamics require several inputs, e.g., charges, masses, mean velocities, and temperatures, as well as, initial and boundary conditions, and then output a number of quantities of interest. Though dimensional analysis and other reduction techniques can be used to reduce the size of the parameter space, plasma physicists and computational scientists often use these simulations to study the relationship between the original input parameters and subsequent output variables. The field of uncertainty quantification (UQ) generally aims to characterize quantities of interest in simulations subject to variability in the inputs. These characterizations often reduce to parameter studies that treat the inherent model as a mapping between inputs p and a specified quantity of interest $g(p)$. Such studies fall under the domain of sensitivity analysis, and several techniques – such as parameter correlations [26], Sobol indices [9], and Morris screening [27] – exist that use a few simulation runs to screen the importance of input variables.

Another approach is to identify important linear combinations of the inputs p and focus parameter studies along these associated directions. Active subspaces [7,28] are defined by important directions in the high-dimensional space of inputs; once identified, scientists can exploit the active subspace to enable otherwise infeasible parameter studies for expensive simulations [29,30]. More precisely, an active subspace is a low-dimensional linear subspace of the set of parameters, in which input perturbations along these directions alter the model's predictions more, on average, than perturbations which are orthogonal to the subspace. The identification of these subspaces allow for global, rather than local, sensitivity measurements of output variables with respect to parameters and often the construction of reduced-order models that greatly decrease the dimension of the input parameter space. In the current context, they may allow one to answer particular physical questions, such as determining which parameters are most influential to the rate of instability or identifying the minimal and maximal values of this rate within a particular parameter regime.

We begin with a description of the gradient-based active subspace method, which has been recently summarized within [7]. Let $p \in P = [-1,1]^m$ denote a vector of model inputs, where m is a positive integer representing the number of parameters, and the space P represents a *normalized* set of parameter values. Namely, we assume that the independent inputs have been shifted and scaled so that they are centered at the origin and possess unit variation. Additionally, we assume the input space is equipped with a probability density function $\psi(p)$ that is strictly positive in the domain of the quantity of interest $g(p)$, zero outside the domain, and is normalized so that $\int_P \psi(p)\, dp = 1$. In practice, ψ identifies the set of input parameters of interest and quantifies their variability. Assume that $g : P \to \mathbb{R}$ is continuous, square-integrable with respect to the weight ψ, and differentiable with gradient vector $\nabla g \in \mathbb{R}^m$, which is also square-integrable with respect to ψ. The active subspace is then defined by the first $n < m$ eigenvectors of the $m \times m$ symmetric positive semi-definite matrix

$$C = \int_P \nabla g(p) \nabla g(p)^T \psi(p)\, dp =: W \Lambda W^T, \tag{6}$$

where the right side of (6) represents the spectral decomposition of C [31,32]. In other words, W represents the orthogonal matrix whose columns w_ℓ, $(\ell = 1, \ldots, m)$ are the orthonormal eigenvectors of C, and Λ is the diagonal matrix of eigenvalues of C, denoted $\lambda_1, \ldots, \lambda_m$. The matrix C represents an average derivative functional which weights input values according to the probability density ψ. Additionally, we assume that the eigenvalues in Λ (each of which must be non-negative) are listed in descending order and the associated eigenvectors are listed within the same column as their corresponding eigenvalues. The eigenvalue λ_ℓ measures the average change in g subject to perturbations in p along the corresponding eigenvector w_ℓ, as they are related by the identity

$$\lambda_\ell = \int_P |\nabla g(p) \cdot w_\ell|^2 \psi(p)\, dp \tag{7}$$

for $\ell = 1, \ldots, m$.

For example, if $\lambda_\ell = 0$, then g is constant along the direction w_ℓ, and directions along which g is constant can be ignored when studying the behavior of g under changes in the parameter space P. Conversely, if the eigenvalue under consideration is large, then we may deduce from (7) that on average g changes considerably in the direction of the corresponding eigenvector. Now, suppose that a spectral gap exists, and the first $n < m$ eigenvalues are much larger than the trailing $m-n$. Let W_1 be the matrix containing the first n columns of W. Then, as we will show below, a reasonable approximation for g is $g(p) \approx h(W_1^T p)$, where h is the projection of g onto the range of W_1, i.e. $h(y) = g(W_1 y)$.

Once the eigendecomposition involving W and Λ in (6) has been determined, the eigenvalues and eigenvectors can be separated in the following way:

$$\Lambda = \begin{bmatrix} \Lambda_1 & 0 \\ 0 & \Lambda_2 \end{bmatrix}, \quad W = \begin{bmatrix} W_1 & W_2 \end{bmatrix} \tag{8}$$

where Λ_1 contains the "large" eigenvalues of C, Λ_2 contains the "small" eigenvalues, and W_k contains the eigenvectors associated with each Λ_k, for $k = 1, 2$. A simple way to differentiate between the "large" and "small" eigenvalues is to list them on a log plot from greatest to least and determine the appearance of a spectral gap. This gap will correspond to differences of at least an order of magnitude, and thus allow one to compartmentalize the greatest eigenvalues within Λ_1 and the remaining, lesser eigenvalues in Λ_2. A more systematic method of choosing the number of eigenvalues to store within Λ_1 can also be utilized, as developed in [7].

With the decomposition (8), we can represent any element p of the parameter space by

$$p = \underbrace{W W^T}_{=I} p = W_1 \underbrace{W_1^T p}_{=q} + W_2 \underbrace{W_2^T p}_{=r} = W_1 q + W_2 r. \tag{9}$$

Thus, evaluating the quantity of interest at p is equivalent to doing so at the point $W_1 q + W_2 r$, and we may approximate $g(p)$ using

$$g(p) = g(W_1 q + W_2 r) \approx g(W_1 q) = g(W_1 W_1^T p) =: h(W_1^T p).$$

By the definition of W_1 and W_2, it is clear that small perturbations in r will not, on average, alter the values of g. However, small perturbations in q will, on average, change g significantly. For this reason the outputs of W_1 are defined to be the *active subspace* of the model and the outputs of W_2 are the corresponding *inactive subspace*. The linear combinations that generate these subspaces then represent the contributions of differing parameters in the model and describe the sensitivity of the quantity of interest with respect to parameter variations.

In general, the eigenvalues and eigenvectors of C defined by (6) can be well-approximated computationally, using finite difference methods and Monte Carlo sampling. Though we only briefly outline the method below, full details can be found in [7] (Algorithm 3.1) and [28]. The numerical algorithm can be described concisely as follows:

Table 1
Two-stream instability parameters and their baseline values.

Two-stream instability		
Parameter	Quantity	Baseline
α	Perturbation size	N/A
k	Perturbation wavenumber	0.5
μ	Mean velocity	0
σ^2	Scale parameter	1
p	Parameter vector	$[p_1, p_2, p_3] \propto [k, \mu, \sigma^2]$

Table 2
Bi-Maxwellian parameters and their baseline values.

Double beam			Bump-on-tail		
Param.	Quantity	Baseline	Param.	Quantity	Baseline
α	Perturbation size	N/A	α	Perturbation size	N/A
k	Perturbation wavenumber	0.5	k	Perturbation wavenumber	0.5
$\mu_1,\ \mu_2$	Mean velocities	0, 4	$\mu_1,\ \mu_2$	Mean velocities	0, 4
$\sigma_1^2,\ \sigma_2^2$	Thermal velocities	0.5, 0.5	$\sigma_1^2,\ \sigma_2^2$	Thermal velocities	0.25, 0.25
β	Relative strength	0.5	β	Relative strength	0.8
Parameter vector	$p = [p_1, p_2, p_3, p_4, p_5, p_6] \propto [k, \mu_1, \mu_2, \sigma_1^2, \sigma_2^2, \beta]$				

1. Draw N parameter samples $\{p_j\}_{j=1}^N$ independently according to the density ψ.
2. For each parameter sample p_j, compute the gradient $\nabla_p g_j = \nabla_p g(p_j)$
3. Approximate the matrix C by the finite sum
$$C \approx \hat{C} = \frac{1}{N}\sum_{j=1}^{N}(\nabla_p g_j)(\nabla_p g_j)^T$$
4. Compute the corresponding eigendecomposition $\hat{C} = \hat{W}\hat{\Lambda}\hat{W}^T$.

We note that the last step is equivalent to computing the Singular Value Decomposition (SVD) of the matrix

$$\frac{1}{\sqrt{N}}\left[\nabla_p g_1 \dots \nabla_p g_N\right] = \hat{W}\sqrt{\hat{\Lambda}}\hat{V},$$

where it can be shown that the singular values are the square roots of the eigenvalues of $\hat{C}$ and the left singular vectors are the eigenvectors of $\hat{C}$. The SVD method of approximating $\hat{C}$ was developed first in [33] and further utilized to study the global sensitivity of parameters within a variety of scientific models [34–39].

Once $\hat{W}$ and $\hat{\Lambda}$ are computed, we further decompose the eigenspace into their active and inactive portions, namely $\hat{W}_1$ and $\hat{W}_2$, which correspond to the set of eigenvectors associated with the large eigenvalues along the diagonal of $\hat{\Lambda}_1$ and the small eigenvalues along the diagonal of $\hat{\Lambda}_2$, respectively. In practice and as we will find below, many systems possess a one-dimensional active subspace, so that $\hat{\Lambda}_1 \in \mathbb{R}$ and $\hat{W}_1 = w \in \mathbb{R}^m$. In such a scenario, the values of the vector w represent the weights in a linear combination of the input parameters along which the quantity of interest is most volatile. In this way, the entries of w describe the relative importance of the parameters with respect to this quantity. For instance, if $w_2 \gg w_1$, then we generally expect $g(p)$ to vary more when the second entry of p is altered from the w direction than when the first entry of p is altered. Similarly, if say $w_3 \approx 0$ then $g(p)$ does not change much on average when the third entry of p is altered. With this information, the ultimate goal is to produce a model possessing reduced dimensional dependence, and this can be achieved by using a *sufficient summary plot*. In particular, if the active subspace is one-dimensional, then we have identified the single direction in the parameter space along which g is most variable, and hence, the Monte Carlo sample points $\{p_j\}_{j=1}^N$ can be used to construct an approximate model h along this direction, which is given by $w^T p$. To create the reduced model, a simple linear fit, or if greater precision is required, a nonlinear least-squares curve fit, can be used. In the following section, we focus on using these tools in conjunction with numerical simulations of the dispersion relation in order to (i) identify the physical parameters that are most influential and (ii) generate nonlinear, low-dimensional models for the growth rate of plasma instabilities.

4. Computational methods

Now that the active subspace method has been described, we will demonstrate its utility for simulations of the instability rate by applying the aforementioned algorithm. Of course, prior to applying the procedure for computing a reduced model, we must first decide how to represent the original computational model; that is, how to approximate solutions of (1). In our simulations the quantity of interest is the instability growth rate γ, and this must be computed from a set of normalized input parameters,

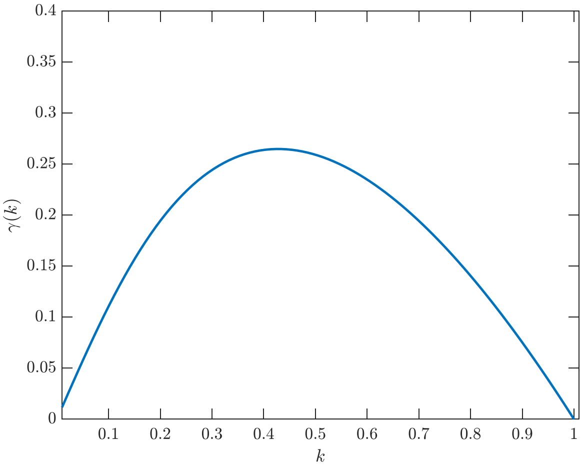

Fig. 1. *Two-Stream instability:* The growth rate as a function of k, indicating peak at $(k,\gamma) = (0.4241, 0.2649)$. The function matches that represented within [41].

e.g. $p = [p_1, p_2, p_3] \propto [k, \mu, \sigma^2]$ for the Two-Stream distribution, where the symbol $\propto$ is merely used to abbreviate the linear relationship between the original variables (k, μ, σ^2) and their normalized counterparts (p_1, p_2, p_3) given by (10) below. Hence, the computational model is expressed as a specific function g so that $\gamma = g(p)$. For the remainder of the paper, the function $g(p)$ merely represents the process of approximating the exponential growth rate of a plane wave solution of the linearized Vlasov–Poisson system (1) by computing roots of the dispersion relation (2) associated with a specific steady state and its normalized parameters p. We note that the dispersion relation solver requires a numerical approximation of the plasma Z-function [40] to compute the temporal frequency ω that satisfies $\varepsilon(k,\omega) = 0$ for a specified value of k.

Notice that gradients of the growth rate are also required to implement the active subspace method. Though one can more easily employ a finite difference scheme with a sufficiently small step size (e.g., $\Delta = 10^{-6}$) to approximate these gradients from two samples of γ, an explicit representation of partial derivatives of γ as a function of system parameters can be obtained by implicit differentiation in (2). For example, taking a derivative with respect to k within (2) and simplifying yields

$$\frac{\partial \gamma}{\partial k} = -\mathrm{Im}\left(\frac{\int \frac{f'_{eq}(v)v}{(v-\omega/k)^2}\, dv + \int \frac{f'_{eq}(v)}{v-\omega/k}\, dv}{\int \frac{f'_{eq}(v)}{(v-\omega/k)^2}\, dv} \right),$$

which can be computed for any set of parameters. Analogous formulas for the derivatives of γ with respect to other parameters follow in the same manner. Hence, we will evaluate explicit formulas for the partial derivatives of γ from the random samples in order to approximate the necessary gradients. Thus, each parameter sample merely requires one root of the dispersion relation to construct the gradient of the growth rate mapping with respect to the normalized model parameters.

Additionally, in forthcoming simulations each sample is chosen so that every normalized parameter is uniformly distributed between -1 and 1, i.e. $p_j \sim \mathcal{U}([-1,1]^m)$ for $j = 1, \dots, N$, so that $\psi(p) = 2^{-m}$. In order to map this normalized parameter space onto the physically-relevant range of parameter values, we use the linear mapping

$$p_{\text{range}} = \frac{1}{2}\left(\mathrm{diag}(u - \ell)p_j + (u + \ell)\right), \tag{10}$$

for the random samples $\{p_j\}_{j=1}^N$, where u and ℓ are vectors containing the upper and lower bounds on the original parameters, respectively. Thus, the resulting vector p_{range} represents the physical parameter values input to the model. For our purposes, the upper and lower limits, u and ℓ are defined to incorporate a specific percentage (e.g., 1%, 5%, 25%) above and below the baseline values given in Tables 1 and 2, respectively. For instance, in performing a 1% perturbation from the baseline parameter vector b, we take $u = 1.01b$ and $\ell = 0.99b$. If a baseline value is identically zero, as in the case of μ, then for a 1% perturbation we take $u = 0.01$ and $\ell = -0.01$.

In the next section, we provide results from simulation studies of the Two-Stream and Bi-Maxwellian distributions. All numerical simulations were conducted in MATLAB using a high-performance computing node with a 3.0 GHz Skylake 5118 24-Core processor and 192 GB of RAM. The code used to generate the results in this section is available at

https://github.com/sterrab/GSA_PlasmaInstabilities.git [42].

Average simulation times ranged from two to five seconds to generate 2^9 trials. The global sensitivity analysis provides an explicit representation of the growth rate $\gamma = g(p)$. As mentioned in the previous section, if a one-dimensional active subspace arises then such a multivariate function can be well-approximated as a scalar function $h(y)$, where $y = w^T p$ and w is the weight vector corresponding to the independent parameters. In this case, $w^T p$ is merely a linear combination of the weighted parameters p. These parameter weights w and functions $h(y)$ are presented for the various global sensitivity analyses along with the associated sufficient summary plots.

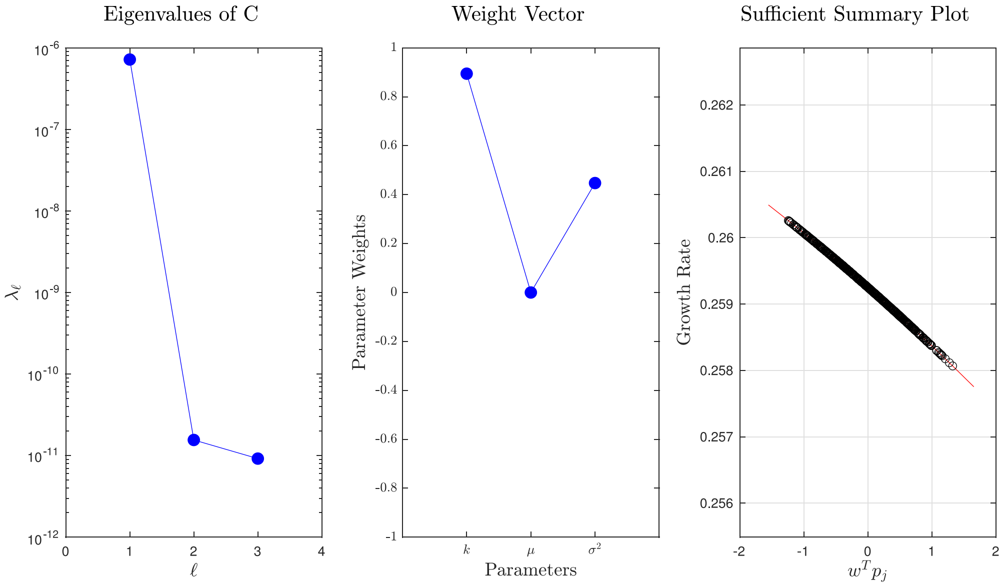

Fig. 2. *Two-Stream Instability:* Global sensitivity analysis (1%) indicating the eigenvalues (left), parameter weights (center), and sufficient summary plot (right) of the one-dimensional active subspace, which represents $\eta_1 = 99.99\%$ of the total variation.

5. Computational results

The active subspace method was numerically implemented for the linear parameter regime by computationally approximating roots of the dispersion relation $\varepsilon(k,\omega) = 0$ for ω given the parameter value k and defining the output quantity of interest to be $\gamma = \mathrm{Im}(\omega)$. As the dispersion relation further depends upon parameters within the steady state distribution, the resulting growth rate will also be a function of these quantities. Throughout the simulation study, the chosen parameters are merely representative of a specific physical environment, and we note that any selection of parameter values can be utilized within the global sensitivity analysis.

In order to verify that our simulations match those of previous computational (but, not parameter) studies, we first performed a series of simulations for the Two-Stream instability with $\mu = 0$ and $\sigma^2 = 1$ and reproduced known results. In particular, Fig. 1 displays the resulting growth rate γ as a function only of the wavenumber k and results in outputs identical to that of [41].

5.1. *Two-Stream instability*

We begin by studying the behavior of spatiotemporal perturbations from the Two-Stream distribution, given by

$$f_{TS}(v;\mu,\sigma^2) = \frac{1}{\sqrt{2\pi\sigma^3}}|v-\mu|^2 \exp\left(-\frac{1}{2\sigma^2}|v-\mu|^2\right).$$

Its associated dispersion relation (Appendix B) is

$$\varepsilon_{TS}(k,\omega) = 1 - \frac{1}{\sigma^2 k^2}\left[1 - 2A(u)^2 + 2\left(A(u) - A(u)^3\right) Z(A(u))\right],$$

where $u = \omega/k$, $A(u) = \frac{1}{\sqrt{2\sigma^2}}(u-\mu)$, and $Z(\cdot)$ is the plasma Z-function defined by (4). As the nonlinear growth of this instability has been shown numerically [41,43], this three-parameter distribution serves as a useful test case prior to investigating more complex distributions. Within these simulations, the parameters k, μ, and σ^2 are shifted and scaled to create the normalized parameter vector $p = [p_1, p_2, p_3] \propto [k, \mu, \sigma^2]$, and their baseline values are set at $k = 0.5, \mu = 0$, and $\sigma^2 = 1$. The simulation study includes variations of 1%, 15%, 25%, and 50% of these nominal parameter values, and a total number of 512 parameter samples were drawn in parallel. We note that taking, for instance, $\sigma^2 \in [0.5, 1.5]$ in the dimensionless framework is equivalent to considering perturbations of up to 50% of the thermal velocity of the plasma.

With the simulation parameters complete, we first perform a 1% perturbation simulation using the active subspace algorithm. Fig. 2 displays three distinct panels of the resulting decomposition — the eigenvalues (listed in descending order) $\lambda_1 > \cdots > \lambda_3 = \mathrm{diag}(\hat{\Lambda})$ of the covariance matrix C, the active subspace weight vector w, and a sufficient summary plot detailing the dependence of the output variable $\gamma \approx h(y)$ on the linear combination of input parameters $y = w^T p$ with each of the N data points representing a Monte Carlo sampling value p_j, $j = 1, \ldots, N$.

From the first panel, we can clearly identify a large spectral gap between the first and second eigenvalues. The second panel of the figure displays the eigenvector $w = [0.89, 3.1 \times 10^{-5}, 0.45]^T$ corresponding to the maximal eigenvalue λ_1, and it can be seen that

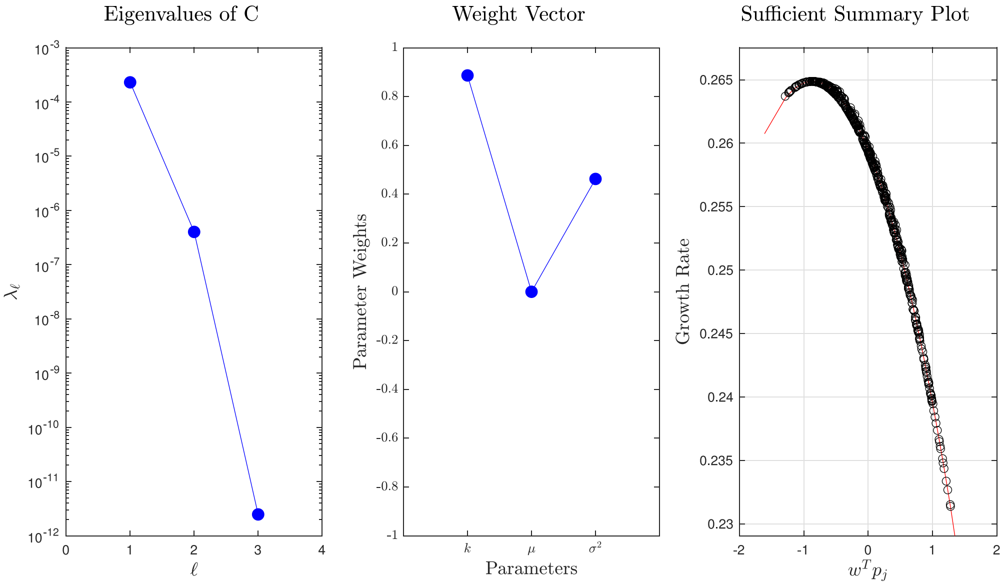

Fig. 3. *Two-Stream Instability:* Global sensitivity analysis (15%) indicating the eigenvalues (left), parameter weights (center), and sufficient summary plot (right) of the one-dimensional active subspace, which represents $\eta_1 = 99.83\%$ of the total variation.

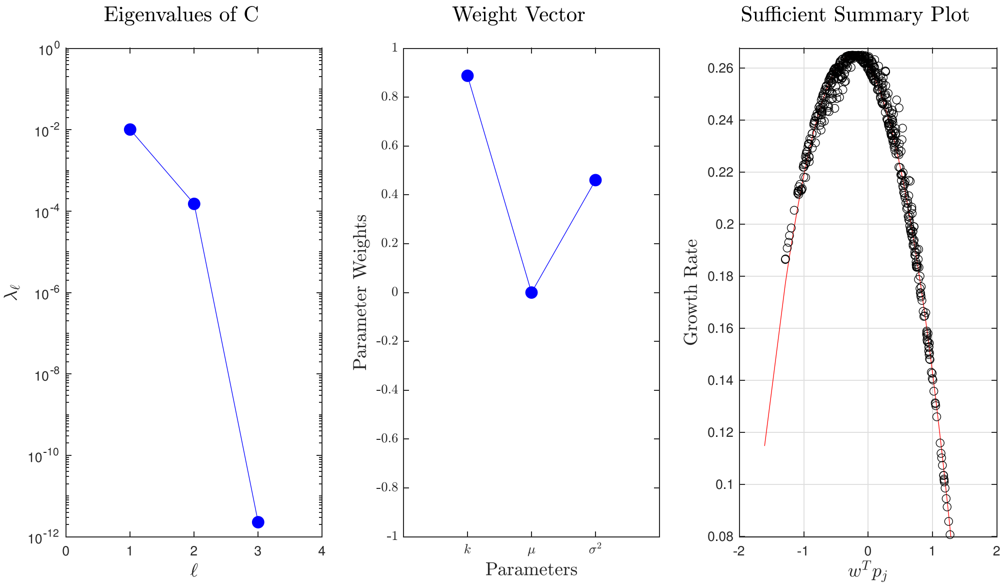

Fig. 4. *Two-Stream Instability:* Global sensitivity analysis (50%) indicating the eigenvalues (left), parameter weights (center), and sufficient summary plot (right) of the one-dimensional active subspace, which represents $\eta_1 = 98.53\%$ of the total variation.

two parameters possess associated weights greater than 0.4, while the remaining parameter possesses a negligible weight. Hence, small perturbations in the former parameters, namely k and σ^2, will significantly alter the value of $\gamma = g(p)$, as they are the most heavily weighted. Contrastingly, changes within the remaining parameter μ, whose weight is near zero, will not have an appreciable affect on γ. Intuitively, the effect on γ of changing μ should be negligible as translations by μ in the velocity distribution function will not influence the growth rate. This idea can be deduced from (2) in noticing that a change of variable $x = v - \mu$ in the dispersion relation integral will only alter $\mathrm{Re}(\omega)$ and not $\mathrm{Im}(\omega)$.

Finally, the third panel contains a plot of the quantity of interest $\gamma = g(p) \approx h(w^T p)$. The horizontal axis contains values of the first active variable $y = w^T p$, which represents a linear combination of the normalized parameters p with weights given by entries of the first active variable vector w. This panel displays the linear functional form of the active subspace decomposition and shows a clear trend, namely that the growth rate γ is a decreasing function of the active variable and can be well approximated by a linear

Table 3
Two-Stream Instability Parameter Weights with $p \propto [k, \mu, \sigma^2]$. Notice that the weight w_1 associated to k is decreasing with the parameter variation from baseline values, while that of σ^2, namely w_3, increases in magnitude. Hence, the wavenumber becomes less influential as the parameter space grows, and the scale parameter (proportional to the thermal velocity) more so.

Variation (%)	Parameter weights $w^T p = w_1 p_1 + w_2 p_2 + w_3 p_3$		
	w_1	w_2	w_3
1	0.8948	3.065×10^{-5}	0.4485
5	0.8936	-1.505×10^{-5}	0.4494
10	0.8910	-5.457×10^{-6}	0.4540
15	0.8866	4.384×10^{-7}	0.4625
20	0.8858	1.074×10^{-7}	0.4641
25	0.8824	2.497×10^{-7}	0.4704
50	0.8877	1.087×10^{-6}	0.4604

function of y. The linearity of this relationship is expected as a 1% variation in parameters constitutes a small perturbation from their baseline values, and is similar to conducting a local sensitivity analysis near this point in order to determine the line of best fit. As the entries of the weight vector corresponding to k and σ^2 are positive ($w_1, w_3 > 0$), this further implies that the growth rate is decreasing in these parameters, due to the decreasing nature of the functional approximation within the third panel. Here, the growth rate is approximated as

$$\gamma_{TS} \approx h\left(0.89p_1 + 3.1 \times 10^{-5} p_2 + 0.45p_3\right),$$

where

$$p_1 = 200(k - 0.5), \qquad p_2 = 100\mu, \qquad p_3 = 100(\sigma^2 - 1)$$

are determined by inverting (10) for each parameter, and h is the linear function defined by

$$h(y) = -0.0008y + 0.2592.$$

Simplifying these expressions, we can write an explicit representation for the growth rate in terms of the original parameters as

$$\gamma_{TS}(k, \mu, \sigma^2) \approx -0.0008\left(178(k - 0.5) + 0.003\mu + 45(\sigma^2 - 1)\right) + 0.2592. \tag{11}$$

This expression can then be used in lieu of evaluating (2) and produces a low-dimensional, inexpensive surrogate model for evaluation of the rate of instability. Furthermore, as this quantity is decreasing in both the wavenumber and the scaling parameter, (11) shows that a more-focused pair of beams or reduced perturbation frequency will give rise to greater instability, while a less concentrated distribution or greater initial frequency will lessen the rate of instability.

The results of additional simulations corresponding to 15% and 50% variations are displayed in Figs. 3–4. These plots include the eigenvalues on the left panel, the entries of the parameter weight vector w of the first eigenvector in the center panel, and the sufficient summary plot of the one-dimensional active subspace in the right panel. Additionally, the reduced dimension approximation, calculated as

$$\eta_1 = \frac{\lambda_1}{\sum_{i=1}^{3} \lambda_i}$$

is included in the caption of each figure to demonstrate the percentage of the total variation captured by the one-dimensional subspace. This quantity is analogous to the eigenvalue ratio used in Principal Component Analysis (PCA). Hence, (11) can be used to compute the growth rate to over 99% accuracy over the parameter space defined by a 1% variation from baseline values.

As shown by the sufficient summary plot, the one-dimensional active subspace changes from linear to quadratic for the simulations presented in Figs. 2–4. The total variation captured by this approximation decreases as the parameter variations are increased, from $\eta_1 = 99.99\%$ for the 1% variational study (Fig. 2) to $\eta_1 = 98.53\%$ for the 50% study (Fig. 4).

Table 3 includes the parameter weights and corresponding $y = w^T p$ scalar variable for the one-dimensional subspace. The exact polynomial fits are included in Table 4 and plotted in Fig. 5. With larger variations, the coefficient of the quadratic term increases in magnitude from -3.3×10^{-5} for the 1% simulation to -8×10^{-2} for the 50% simulation. This is expected as a first-order approximation is less informative away from baseline values. However, even within the 50% simulation the linear term dominates as in Figs. 4 and 5.

Moreover, the spectral gap decreases as the variation percentage increases, displaying a loss in the amount of information that can be captured by using only a one-dimensional approximation along the direction of greatest output fluctuation. Though the disappearance of the spectral gap is not visually documented within these figures, a greater variation in baseline values, say 80%, does begin to show such differences. In particular, the eigenvalues begin to cluster, and this reduces the amount of variation contained within a one-dimensional active subspace decomposition. More specifically, $\eta_1 \approx 90\%$ for the 80% variation from baseline values, so the information captured within a single active variable continues to decrease. Instead, a two-dimensional decomposition

Table 4
Two-stream instability coefficients.

Variation (%)	Polynomial fit $h(w^T p) = h(y) = a_2 y^2 + a_1 y + a_0$		
	a_2	a_1	a_0
1	-3.2899×10^{-5}	−0.0008	0.2592
5	−0.0008	−0.004	0.2593
10	−0.003	−0.008	0.2594
15	−0.007	−0.013	0.2595
20	−0.013	−0.017	0.2597
25	−0.020	−0.021	0.2598
50	−0.080	−0.038	0.2606

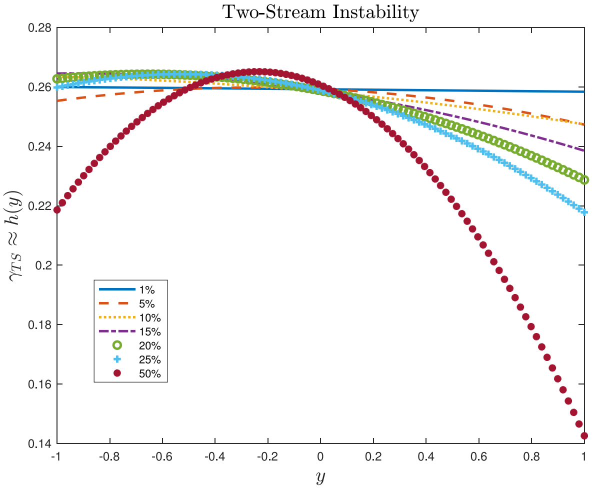

Fig. 5. Two-Stream instability 2nd-order polynomial fits.

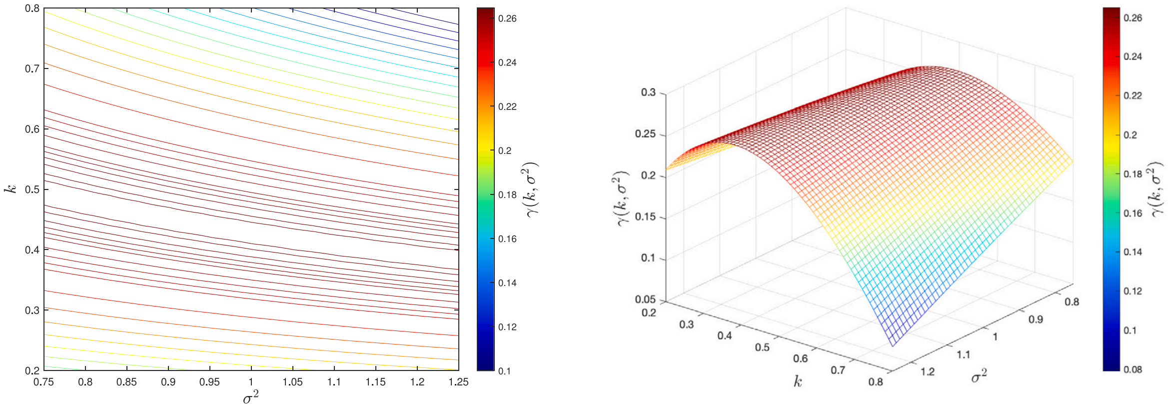

Fig. 6. Level curves (left) and three-dimensional plot (right) of the growth rate $\gamma(k, \sigma^2)$ as a function of the wavenumber and scale parameter. Each parameter is varied by 25% of its baseline value.

can be used to retain a suitable degree of variation in the values of the growth rate, and we will revisit this concept for a more pronounced change in the eigenvalues within a later section.

Alternatively, because the growth rate is insensitive to changes in the mean parameter μ, we can more easily visualize it as a function of the remaining two parameters of the steady state. In Fig. 6 we display a plot of the growth rate $\gamma(k, \sigma^2)$ as a function of the wavenumber and scale parameter with $\mu = 0$ fixed. Additionally, the level curves are displayed and the approximation of the weight vector w is orthogonal to these curves near their baseline values. For each of the parameter variations, the active subspace method allows for the construction of an inexpensive computational approximation and an explicit analytic formula to well approximate the growth rate as a function of model parameters.

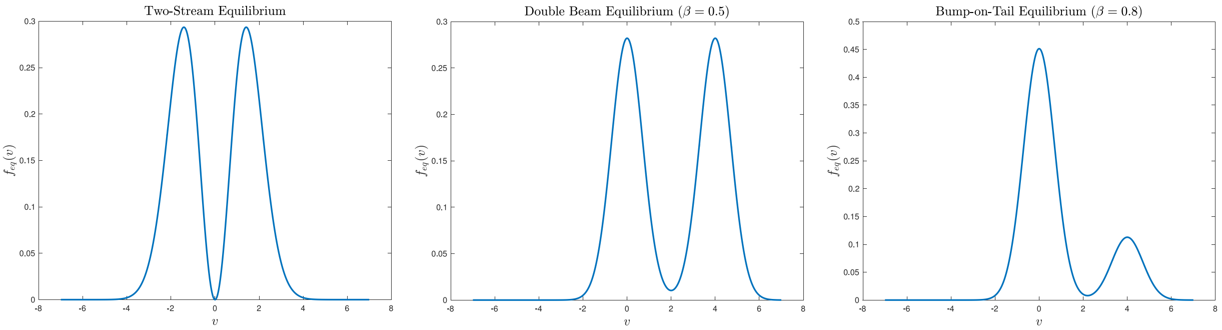

Fig. 7. Two-Stream (left) and Bi-Maxwellian distributions for $\beta = 0.5$ (center) and $\beta = 0.8$ (right).

5.2. *Bi-Maxwellian distribution*

Next, we study the resulting behavior of unstable perturbations from the Bi-Maxwellian distribution, given by

$$f_{BM}(v;\mu_1,\mu_2,\sigma_1^2,\sigma_2^2,\beta) = \frac{\beta}{\sqrt{2\pi\sigma_1^2}}\exp\left(-\frac{1}{2\sigma_1^2}|v-\mu_1|^2\right) + \frac{1-\beta}{\sqrt{2\pi\sigma_2^2}}\exp\left(-\frac{1}{2\sigma_2^2}|v-\mu_2|^2\right), \tag{12}$$

with the constraint $0 < \beta < 1$. The associated dispersion relation for this state (Appendix B) is given by

$$\varepsilon_{BM}(k,\omega) = 1 + \frac{\beta}{\sigma_1^2 k^2}\left[1 + A_1(u)Z(A_1(u))\right] + \frac{1-\beta}{\sigma_2^2 k^2}\left[1 + A_2(u)Z(A_2(u))\right],$$

where $u = \omega/k$,

$$A_i(u) = \frac{1}{\sqrt{2\sigma_i^2}}\left(u - \mu_i\right)$$

for $i = 1, 2$, and $Z(\cdot)$ is again defined by (4).

As before, the parameters (now $k, \mu_1, \mu_2, \sigma_1^2, \sigma_2^2$, and β) are shifted and scaled to create the normalized parameter vector $p = [p_1, p_2, p_3, p_4, p_5, p_6] \propto [k, \mu_1, \mu_2, \sigma_1^2, \sigma_2^2, \beta]$, and we will consider two different sets of baseline values: (i) an instability driven by two distinct plasma beams with differing mean velocities but similar spread and strength that we will call the Double Beam Instability and (ii) the well-known Bump-on-Tail instability. The qualitative differences between these states are displayed in Fig. 7. Finally, to close this section we will also construct an approximation for the Bi-Maxwellian growth rate that is global throughout the parameter space.

5.2.1. *Double Beam instability*

In the first case, we investigate the behavior of the growth rate for a double-humped distribution that represents two ionic beams with similar densities and thermal velocities, but different mean velocities. Here, the baseline parameter values are $k = 0.5, \mu_1 = 0, \mu_2 = 4, \sigma_1^2 = 0.5, \sigma_2^2 = 0.5$, and $\beta = 0.5$. As in the previous section, a total number of $N = 512$ samples are drawn in the parameter space.

The simulations included variations of 1%, 5%, 15%, and 25% of these nominal parameter values, with results presented in Figs. 8–11, and the parameter weights for each of the variational studies are included in Table 5. As before, figures feature the eigenvalues on the left panel, the parameter weight vector w in the center panel, and the sufficient summary plot of the one-dimensional active subspace in the right panel. Throughout each of the simulations, we note that the wavenumber k and mean velocity μ_2 are the most influential on the growth rate. Generally, these parameters are negatively correlated with γ, which is typically a decreasing function of the active variable y. However, the growth of the parabolic component of the reduced approximation indicates that a maximal growth rate is achieved within the parameter regimes corresponding to the 15% and 25% variations. Hence, one can maximize or minimize the rate of instability by altering the physical structure of the beams, in this case the initial frequency of the spatial perturbation k and the mean velocity μ_2. Additionally, we see that, even at lower wavenumbers, increasing the mean velocity of the second beam will attenuate the growth rate. Thus, a greater separation of the mean velocities of the electron beams may serve to tame the instability.

The reduced dimension approximation, calculated as

$$\eta_1 = \frac{\lambda_1}{\sum_{i=1}^{6}\lambda_i},$$

is also included in the caption of each figure to demonstrate the percentage of the total variation captured in the one-dimensional subspace. More generally, we define

$$\eta_m = \frac{\sum_{i=1}^{m}\lambda_i}{\sum_{i=1}^{6}\lambda_i}$$

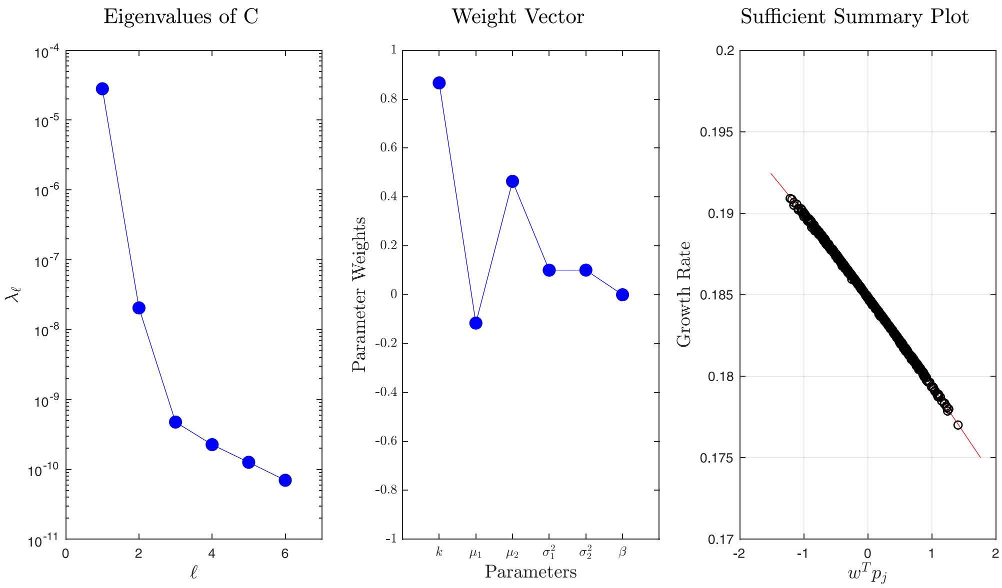

Fig. 8. *Double Beam Instability:* Global sensitivity analysis (1%) indicating the eigenvalues (left), parameter weights (center), and sufficient summary plot (right) of the one-dimensional active subspace, which represents $\eta_1 = 99.92\%$ of the total variation.

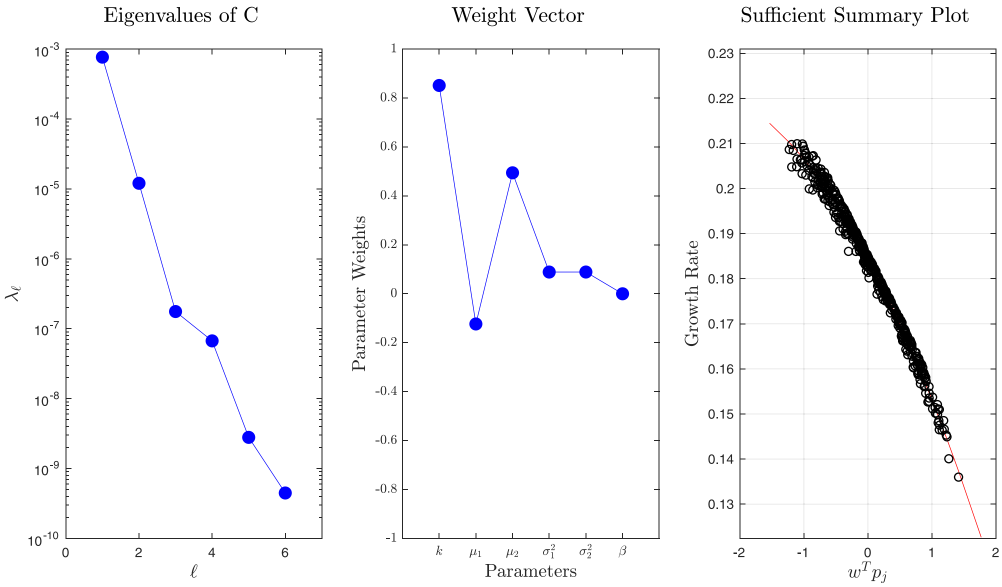

Fig. 9. *Double Beam Instability:* Global sensitivity analysis (5%) indicating the eigenvalues (left), parameter weights (center), and sufficient summary plot (right) of the one-dimensional active subspace, which represents $\eta_1 = 98.42\%$ of the total variation.

for $m = 1, \ldots, 5$ (and $\eta_6 = 1$) to represent the percent variation captured by the m-dimensional active subspace approximation. As can be examined by the sufficient summary plot, the one-dimensional active subspace is linear for the 1% and 5% variational studies (Figs. 8–9). For variations of 15% and greater (Figs. 10–11), the sufficient summary plots become parabolic. This is also observed in Table 6, which displays a larger magnitude of the quadratic coefficient as the variation increases, e.g. -2×10^{-4} for 1% variation and -0.1222 for 25% variation, along with the corresponding transition from linear to parabolic curves in Fig. 12. As expected, the total variation captured by the one-dimensional active subspace drops from $\eta_1 = 99.92\%$ for the 1% variational study (Fig. 8) to $\eta_1 = 92.04\%$ for the 25% study (Fig. 11). Notice that η_1 is decreasing faster than for the Two-Stream study, and we begin to see in Fig. 11 that a one-dimensional active subspace is no longer a strong approximation to the domain of $g(p)$, given the decreasing spectral gap. In comparison, the growth rate as a function of the first and second parameter weight vectors are plotted for both the 1% and 25% simulations in Fig. 13. The corresponding total approximation of the two-dimensional active subspace is $\eta_2 = 99.99\%$

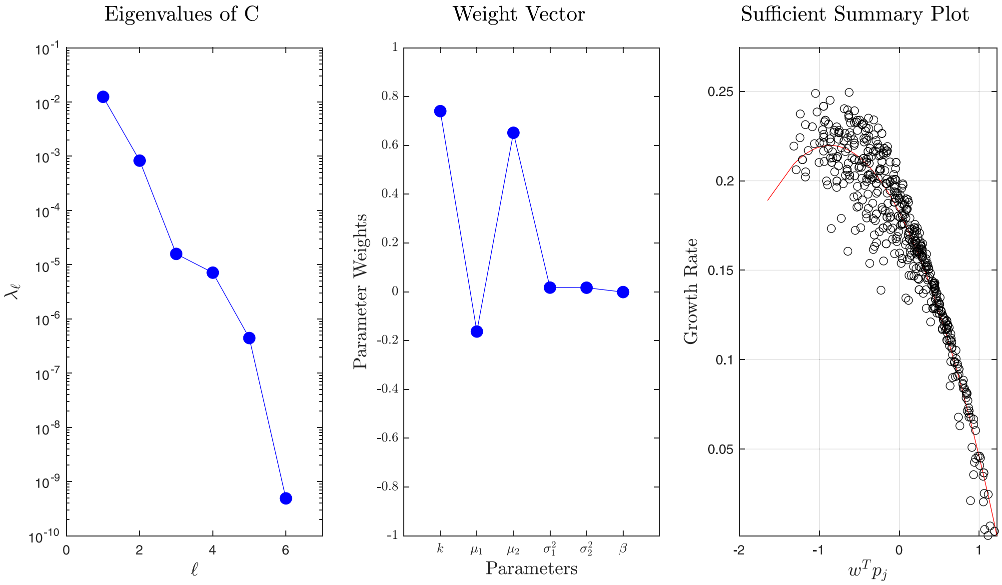

Fig. 10. *Double Beam Instability:* Global sensitivity analysis (15%) indicating the eigenvalues (left), parameter weights (center), and sufficient summary plot (right) of the one-dimensional active subspace, which represents $\eta_1 = 93.60\%$ of the total variation.

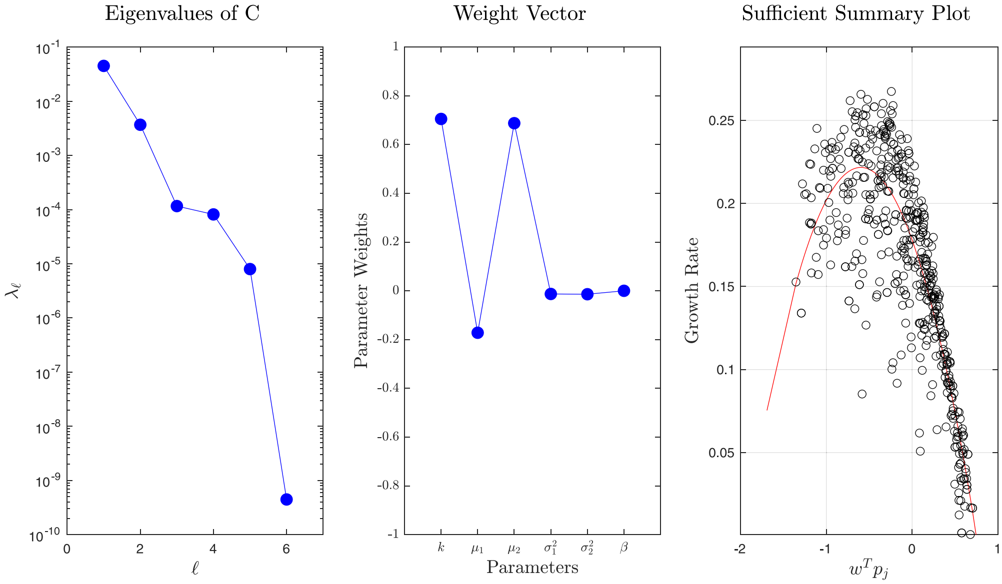

Fig. 11. *Double Beam Instability:* Global sensitivity analysis (25%) indicating the eigenvalues (left), parameter weights (center), and sufficient summary plot (right) of the one-dimensional active subspace, which represents $\eta_1 = 92.04\%$ of the total variation.

for the 1% perturbations and $\eta_2 = 99.58\%$ for the 25% perturbation simulation. Indeed, in the left plot in Fig. 13 representing the 1% simulation, the growth rate as shown by the vertical banded colors does not change along the vertical axis, which represents the second parameter weight vector. On the other hand, for the 25% case in the right plot in Fig. 13, the growth rate can change significantly along both the horizontal and vertical axes, corresponding to the first and second parameter weight vectors.

As for the Two-Stream instability, an explicit approximation of the growth rate can be constructed for each parameter study. For instance, if the normalized parameters are varied by 10% from their baseline value (see Tables 5 and 6) the growth rate is well-approximated by $\gamma_{DB} \approx h(y)$, where

$$y = 0.80p_1 - 0.14p_2 + 0.58p_3 + 0.05p_4 + 0.05p_5 - 0.0002p_6$$

Table 5
Double beam instability parameter weights.

Variation (%)	Parameter weights $w^T p = w_1 p_1 + w_2 p_2 + w_3 p_3 + w_4 p_4 + w_5 p_5 + w_6 p_6$					
	w_1	w_2	w_3	w_4	w_5	w_6
1	0.8666	−0.1159	0.4640	0.1006	0.1009	-4.6×10^{-5}
5	0.8513	−0.1235	0.4943	0.0887	0.0888	−0.0002
10	0.8017	−0.1438	0.5752	0.0539	0.0542	−0.0002
15	0.7404	−0.1629	0.6517	0.0171	0.0167	−0.0012
20	0.7069	−0.1715	0.6860	−0.0076	−0.0095	0.0056
25	0.7051	−0.1719	0.6877	−0.0128	−0.0139	0.0002

Table 6
Double beam instability coefficients.

Variation (%)	Polynomial fit $h(w^T p) = h(y) = a_2 y^2 + a_1 y + a_0$		
	a_2	a_1	a_0
1	−0.0002	−0.0053	0.1848
5	−0.0046	−0.0267	0.1845
10	−0.0213	−0.0550	0.1838
15	−0.05	−0.0866	0.1823
20	−0.0828	−0.1158	0.1786
25	−0.1222	−0.1461	0.1780

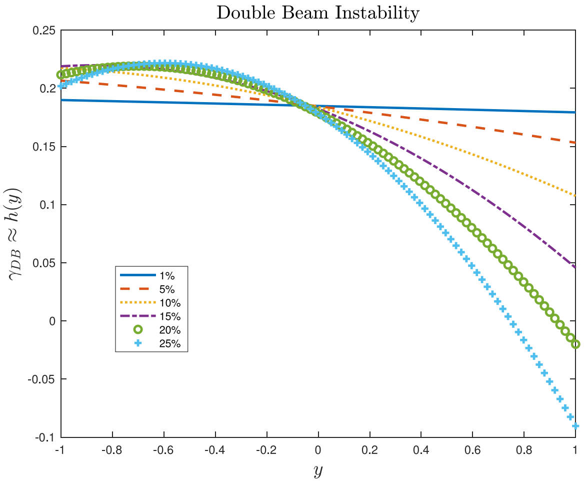

Fig. 12. Double beam instability 2nd-order polynomial fits.

is the active variable that can be represented in terms of the original variables using

$$p_1 = 20(k - 0.5), \qquad p_2 = 10\mu_1, \qquad p_3 = 2.5(\mu_2 - 4),$$
$$p_4 = 20(\sigma_1^2 - 0.5), \qquad p_5 = 20(\sigma_2^2 - 0.5), \qquad p_6 = 20(\beta - 0.5),$$

and h is the quadratic function defined by

$$h(y) = -0.021y^2 - 0.055y + 0.1838.$$

Simplifying y in terms of the original variables yields

$$y = 16(k - 0.5) - 1.4\mu_1 + 1.45(\mu_2 - 4) + (\sigma_1^2 - 0.5) + (\sigma_2^2 - 0.5) - 0.004(\beta - 0.5).$$

This expression can then be inserted into $h(y)$ to produce an explicit function for the growth rate in terms of the original parameters, namely $\gamma_{DB}(k, \mu_1, \mu_2, \sigma_1^2, \sigma_2^2, \beta)$.

5.2.2. Bump-on-Tail instability

In addition to the Double Beam instability of the previous section, we investigate the Bump-on-Tail instability arising from two ionic beams of differing density and mean velocity [44]. Here, the baseline parameter values are $k = 0.5, \mu_1 = 0, \mu_2 = 4, \sigma_1^2 = 0.25, \sigma_2^2 = 0.25$, and $\beta = 0.8$. Similarly, a total number of $N = 512$ samples were drawn in the parameter space.

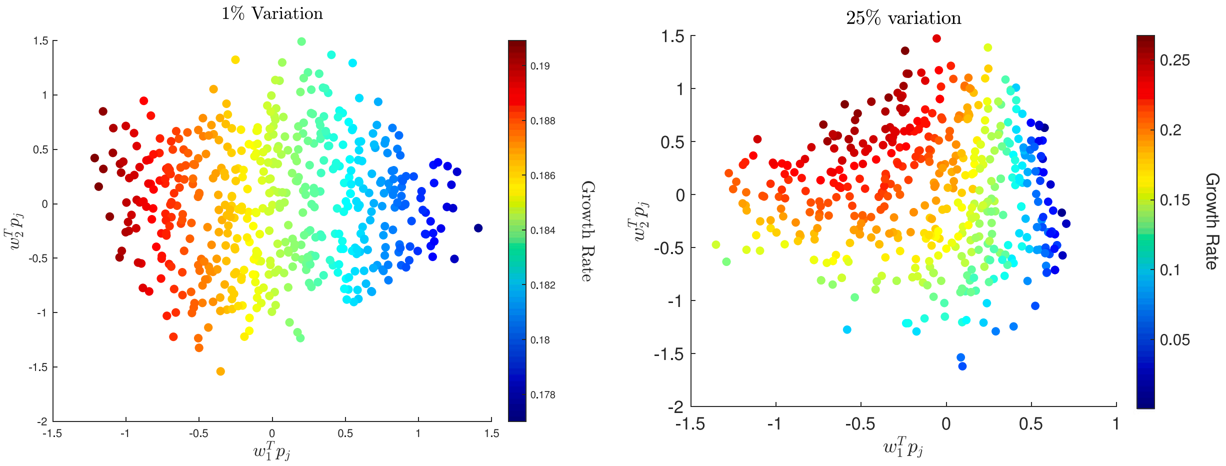

Fig. 13. Two-Dimensional sufficient summary plots for the Double Beam instability: (left) 1% global sensitivity analysis, which represents $\eta_2 = 99.99\%$ of the total variation, and (right) 25% global sensitivity analysis, which represents $\eta_2 = 99.58\%$ of the total variation. Notice that a one-dimensional representation (see Fig. 11) cannot capture the variability expressed in the growth rate as a function of model parameters.

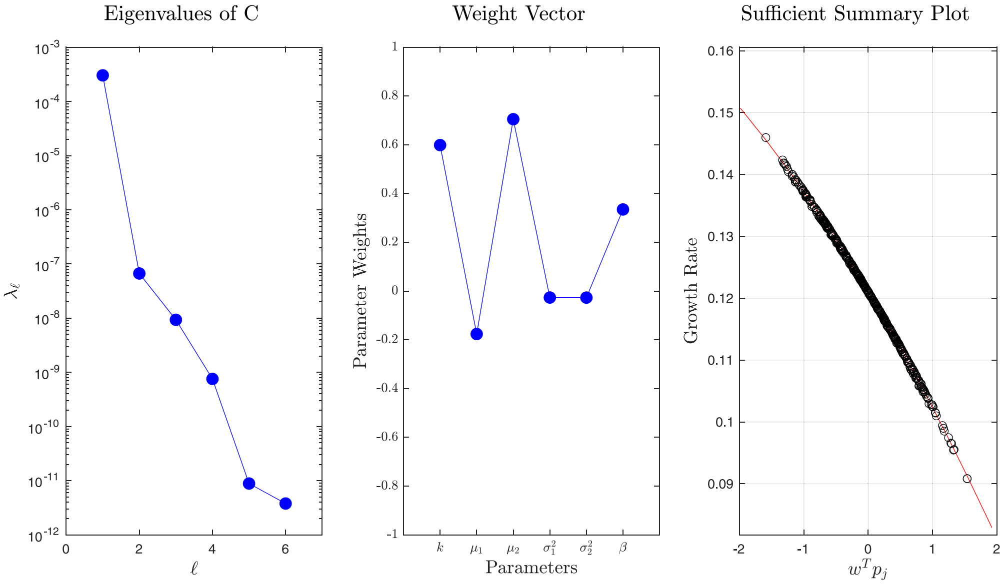

Fig. 14. *Bump-on-Tail instability:* Global sensitivity analysis (1%) indicating the eigenvalues (left), parameter weights (center), and sufficient summary plot (right) of the one-dimensional active subspace, which represents $\eta_1 = 99.97\%$ of the total variation.

The simulations included variations of 1%, 10%, and 25% of these nominal parameter values, with results presented in Figs. 14–16, and parameter weights included in Table 7. As shown in the sufficient summary plot, the one-dimensional active subspace is essentially linear for the 1% variation study (Fig. 14), but becomes parabolic for the 10% variation study and greater (Figs. 15–16). This is also observed in Table 8, which displays an increasing magnitude of the quadratic coefficient as the variation increases, e.g. -1.2×10^{-3} for 1% variation and -0.1308 for 25% variation, as well as in the polynomial fits in Fig. 17 that gradually become more nonlinear with increased parameter variation. The information captured by the one-dimensional active subspace drops from $\eta_1 = 99.97\%$ for the 1% variation study (Fig. 14) to $\eta_1 = 86.83\%$ for the 25% study (Fig. 16). In accordance with the reduced spectral gap, we observe that a one-dimensional active subspace is no longer a strong approximation to the domain of $g(p)$, similar to the 25% variation study of the previous section. As for the Double Beam instability, the wavenumber k and mean velocity μ_2 are the most influential parameters on the growth rate and generally remain negatively correlated with γ. However, the density β of the larger Maxwellian is also moderately influential within this region of the parameter space; hence, the values of γ in the Bump-on-Tail instability will depend on β in a non-negligible manner. As before, the influence of the parabolic component of the reduced approximation for the 10% and 25% variations indicates that a maximal growth rate is achieved within these parameter regimes. Thus, the rate of instability can be suitably increased or decreased by altering the initial frequency of the perturbation

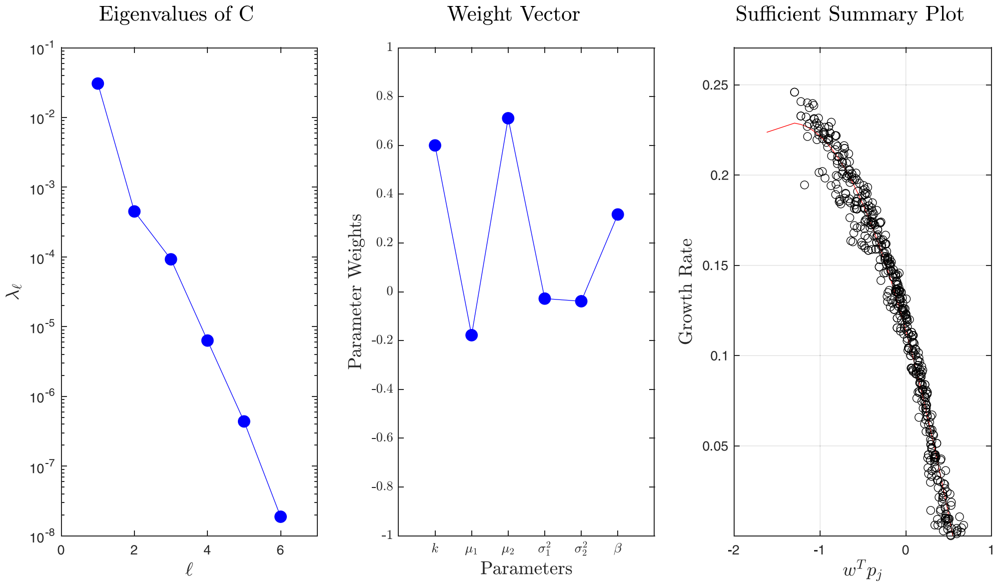

Fig. 15. *Bump-on-Tail Instability:* Global sensitivity analysis (10%) indicating the eigenvalues (left), parameter weights (center), and sufficient summary plot (right) of the one-dimensional active subspace, which represents $\eta_1 = 98.24\%$ of the total variation.

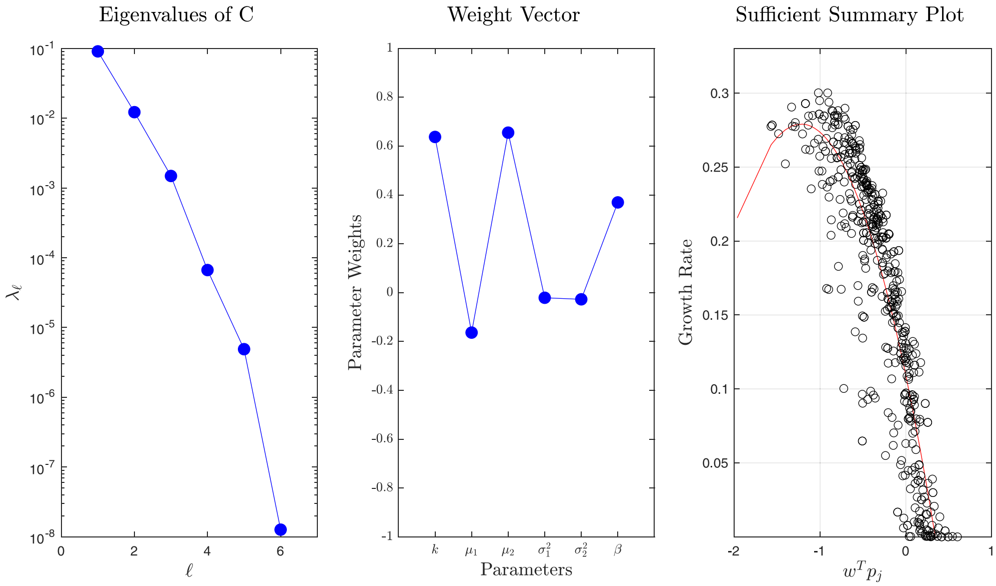

Fig. 16. *Bump-on-Tail Instability:* Global sensitivity analysis (25%) indicating the eigenvalues (left), parameter weights (center), and sufficient summary plot (right) of the one-dimensional active subspace, which represents $\eta_1 = 86.83\%$ of the total variation.

k, the mean velocity μ_2, and the relative density of the larger beam, given by β. More specifically, one can essentially drive the growth rate to zero in this parameter regime by choosing μ_2 or β sufficiently large. That being said, as μ_2 is more influential than β, increasing the thermal velocity of the bump on the tail of the distribution will more easily reduce the growth rate of the instability than proportionately decreasing its density. In addition, the maximal value attained by the growth rate is analogous to that of the Two-Stream instability, and hence these phenomena can manifest with similar intensity. In contrast, we note that the volatility (i.e., the spread) in the values of the growth rate for either of the Bi-Maxwellian distributions is significantly greater than that of the Two-Stream distribution.

Again, an explicit approximation of the growth rate can be constructed for each parameter variation study. For instance, if the normalized parameters are varied by 10% from their baseline values (see Tables 7 and 8) the growth rate is well-approximated by

Table 7
Bump-on-tail instability parameter weights.

Variation (%)	Parameter weights $w^T p = w_1 p_1 + w_2 p_2 + w_3 p_3 + w_4 p_4 w_5 p_5 + w_6 p_6$					
	w_1	w_2	w_3	w_4	w_5	w_6
1	0.5988	−0.1762	0.7049	−0.0265	−0.0268	0.3348
5	0.5902	−0.1808	0.7232	−0.0292	−0.0390	0.3061
10	0.5999	−0.1779	0.7112	−0.0280	−0.0387	0.3168
15	0.6118	−0.1748	0.6990	−0.0258	−0.0350	0.3236
25	0.6375	−0.1637	0.6551	−0.0211	−0.0274	0.3694
Global	0.5876	−0.0579	0.2897	0.0634	0.0431	0.7494

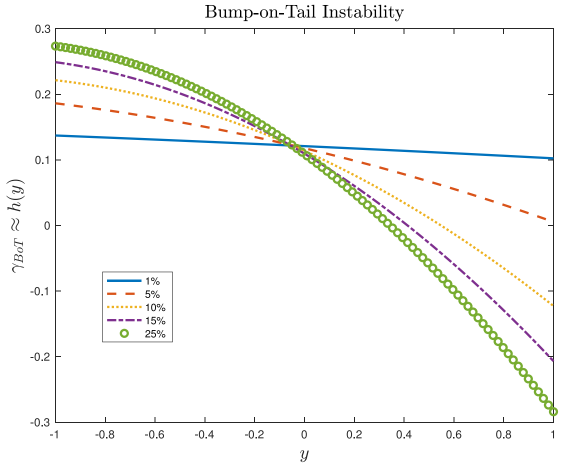

Fig. 17. Bump-on-Tail instability 2nd-order polynomial fits.

$\gamma_{BoT} \approx h(y)$, where

$$y = 0.6p_1 - 0.18p_2 + 0.71p_3 - 0.03p_4 - 0.04p_5 + 0.32p_6$$

is the active variable that can be represented in terms of the original variables using

$$p_1 = 20(k - 0.5), \qquad p_2 = 10\mu_1, \qquad p_3 = 2.5(\mu_2 - 4),$$
$$p_4 = 40(\sigma_1^2 - 0.25), \qquad p_5 = 40(\sigma_2^2 - 0.25), \qquad p_6 = 12.5(\beta - 0.8),$$

and h is the quadratic function defined by

$$h(y) = -0.064y^2 - 0.172y + 0.114.$$

As for the other instabilities, these expressions can then be simplified to produce an explicit function for the growth rate $\gamma_{BoT}(k, \mu_1, \mu_2, \sigma_1^2, \sigma_2^2, \beta)$ in terms of the original parameters.

5.2.3. Global Bi-Maxwellian approximation

Finally, we also consider an approximation of the Bi-Maxwellian instability rate that is global within the parameter space by using a larger range of parameter values to simultaneously represent both of the previous instabilities. Rather than perturb the parameters from a set of baseline values, we instead consider a larger hypercube within which they may vary. Here, the lower and upper bound vectors on the parameters $p \propto [k, \mu_1, \mu_2, \sigma_1^2, \sigma_2^2, \beta]$ are given by

$$\ell = [0.4, -0.1, 3.5, 0.25, 0.25, 0.5]^T \quad \text{and} \quad u = [0.6, 0.1, 4.5, 0.75, 0.75, 0.99]^T,$$

respectively. This implies, for instance, that $\mu_2 = 0.5(p_3 + 8) \in [3.5, 4.5]$ or equivalently, $p_3 = 2\mu_2 - 8 \in [-1, 1]$. Results of the one-dimensional active subspace decomposition are presented in Fig. 18. Unfortunately, because of the differing dominant parameter dependencies of the two instabilities, a single active variable is insufficient to capture their distinct behaviors, though the same variables (k, μ_2, and β) remain the most influential. Thus, a two-dimensional decomposition was also performed (Fig. 19) in order to retain sufficient variation in γ. The associated weight vectors are

$$w_1 = [0.588, -0.058, 0.29, 0.06, 0.04, 0.75]^T,$$

Table 8
Bump-on-tail instability coefficients.

Variation (%)	Polynomial fit $h(w^T p) = h(y) = a_2 y^2 + a_1 y + a_0$		
	a_2	a_1	a_0
1	−0.0012	−0.0174	0.1210
5	−0.0219	−0.0904	0.1178
10	−0.0643	−0.1721	0.1137
15	−0.0884	−0.2279	0.1095
25	−0.1142	−0.2787	0.1090
Global	−0.0263	−0.1348	0.1204

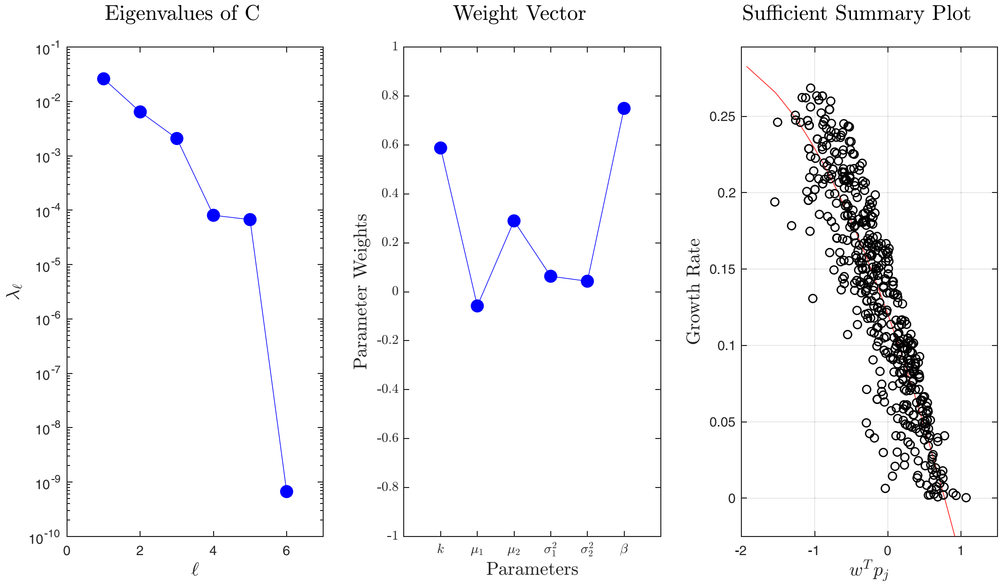

Fig. 18. *Global approximation for Bi-Maxwellian distribution:* Global sensitivity analysis indicating the eigenvalues (left), parameter weights (center), and sufficient summary plot (right) of the one-dimensional active subspace, which represents $\eta_1 = 75.09\%$ of the total variation.

which can be seen in Fig. 18, and

$$w_2 = [-0.567, 0.097, -0.488, 0.143, 0.163, 0.619]^T,$$

representing the two linear combinations of parameters that are most influential on the growth rate. Here, we must note that, unlike in previous sections, w_2 represents the second vector comprising the active subspace, rather than the second entry of the weight vector previously denoted by w. With this, a global parameter approximation $\gamma_G \approx h(y_1, y_2)$ is obtained using a nonlinear least-squares fit to produce a polynomial of desired degree. In this way, we have determined the quadratic surface that best fits the growth rate, given by

$$h(y_1, y_2) = 0.1278 - 0.125y_1 + 0.016y_2 + 0.017y_1y_2 - 0.044y_2^2,$$

where

$$y_1 = w_1^T p \qquad \text{and} \qquad y_2 = w_2^T p.$$

As before, a direct representation of y_1 and y_2, and hence γ_G, in terms of the original parameters can be obtained by inverting (10) for each parameter to find

$$p_1 = 10(k - 0.5), \qquad p_2 = 10\mu_1, \qquad p_3 = 2(\mu_2 - 4),$$
$$p_4 = 4(\sigma_1^2 - 0.5), \qquad p_5 = 4(\sigma_2^2 - 0.5), \qquad p_6 = 4.08(\beta - 0.745).$$

Using the eigenvalues to compute the information contained in this approximation, we find

$$\eta_1 = \frac{\lambda_1}{\sum_{i=1}^{6} \lambda_i} = 0.7509 \qquad \text{and} \qquad \eta_2 = \frac{\lambda_1 + \lambda_2}{\sum_{i=1}^{6} \lambda_i} = 0.9358.$$

Thus, researchers who possess less precise knowledge concerning the range of parameter values within an experiment can utilize this two-dimensional global parameter approximation to capture more than 93% of the variation in γ. Additionally, this approximation

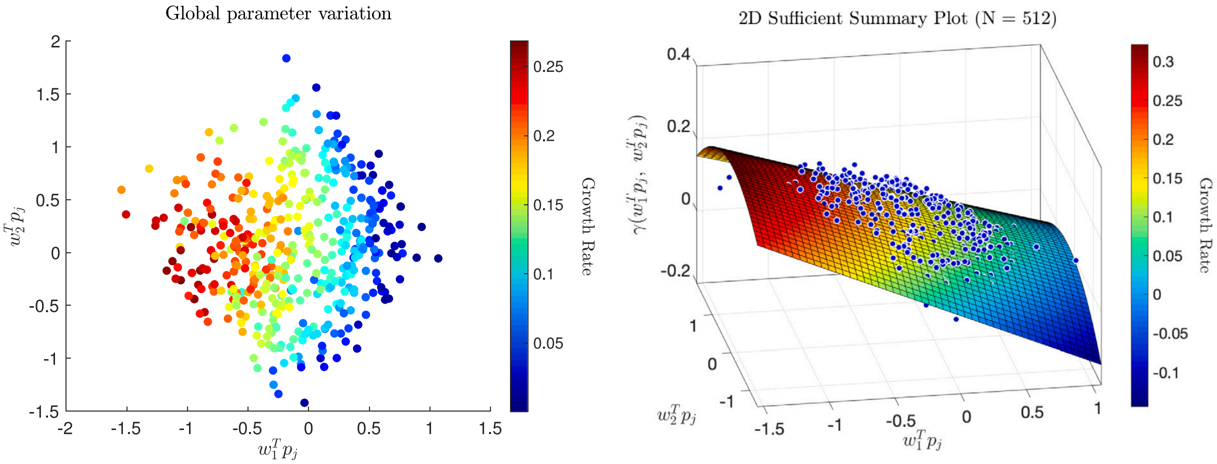

Fig. 19. Two-Dimensional sufficient summary plots for the global approximation of the Bi-Maxwellian distribution: (left) Two-dimensional scatter plot of the outputs and (right) Three-dimensional plot with best multivariate quadratic approximation, representing $\eta_2 = 93.58\%$ of the total variation.

shows that while fluctuations in the beam density β of the larger Maxwellian give rise to the greatest changes throughout the entire parameter space, this effect is attenuated within each of the two featured regimes (Double Beam and Bump-on-Tail).

6. Conclusions

The formulation and implementation of the active subspace method has allowed us to draw a variety of conclusions. First, the parameters of greatest importance to the rate of instability were determined for each steady state. In particular, for both the Double Beam and Bump-on-Tail instabilities, the wavenumber k and mean velocity μ_2 are most influential to the growth rate γ. This, along with the negative correlation of these parameters with γ, indicates that the growth rate can be controlled, and moreover decreased, by increasing the spatial frequency of the initial perturbation or the mean velocity of the second beam. Hence, the linear instability can be tamed by utilizing a high frequency spatial perturbation or suitably separating the mean velocities of the beams.

For the Bump-on-Tail instability, one might further view this result through the lens of a transition from an unstable distribution to a stable one, namely the Maxwellian equilibrium. In particular, a variety of parameter limits, e.g. $\beta \to 1$, $\sigma_2^2 \to \infty$, or the combination of $\mu_2 \to \mu_1$ and $\sigma_2^2 \to \sigma_1^2$, induce the Bi-Maxwellian distribution $f_{eq}(v)$ given by (12) to converge to a normalized Maxwellian with mean velocity μ_1 and thermal velocity σ_1^2. The question then becomes, which of these limits drives the greatest reduction in the rate of instability as it transitions from positive to negative values. Indeed, as Figs. 14–16 demonstrate, separating the velocities of the beams, i.e. pushing the bump further down the tail of the distribution, by increasing μ_2 achieves a greater reduction in the growth rate than (i) decreasing the relative strength of the bump by increasing β or (ii) increasing the thermal velocity by widening the variance and increasing σ_2^2. This is somewhat counterintuitive, as the well-known Penrose criterion [25] is known to imply the linear stability of this equilibrium when the velocity spread between the Maxwellians is sufficiently close. However, as determined by the active subspace analysis, the rate of instability γ is actually reduced by further separation of the velocity spread once the mean velocities of the Maxwellians are already largely separated (e.g., for $\mu_1 \approx 0$ and $\mu_2 \approx 4$). Such a discrepancy may also serve to highlight the differences in behavior between solutions of the linear and nonlinear Vlasov–Poisson system. For instance, though our analysis demonstrates that an increase in the wavenumber will generally decrease the rate of instability arising from the dispersion relation, this need not occur for the full nonlinear plasma model. Indeed, due to the coupling of different spatial modes within the nonlinear system, an unstable equilibrium perturbed at a spatial frequency outside of the instability range may still exhibit exponential growth. Hence, further investigation of the nonlinear dynamics of the Vlasov–Poisson system, rather than the linear response of solutions to a sufficiently small perturbation wave, is certainly warranted.

Next, the extremal values of the growth rate were computed on these intervals, and they demonstrate that the intensity of the Bump-on-Tail or Double Beam instability is similar to that of the Two-Stream instability, as the attained growth rates are all around $\gamma \approx 0.25$ in this dimensionless system. Hence, previous indications [16] that the latter instability must occur with greater intensity or arise on faster timescales may not hold when fluctuations occur in the mean velocities or density of the particle beams, or when differing wavenumbers are considered. That being said, it is clear from our simulations that the instabilities arising from the Bi-Maxwellian distribution possess greater variability in their rates of growth than does the Two-Stream Instability.

Finally, using the dispersion relation, we were able to construct an analytic representation of the growth rate as a function of model parameters for both the Two-Stream and Bi-Maxwellian distributions. The dispersion-based growth rate solver enabled accurate, efficient, and inexpensive simulations even for large parameter variations, such as the 20%, 25%, and 50% simulation cases. Though the one-dimensional approximations begin to break down as the variation percentage is increased beyond $25-50\%$, two-dimensional active subspace approximations were able to retain the overwhelming majority of the variability contained in the growth rate. In particular, simulations of the Two-Stream instability provided the knowledge that γ is essentially independent of the mean velocity μ and allowed for an inexpensive, reduced decomposition with high accuracy. Additionally, simulations of the Double Beam and Bump-on-Tail instabilities demonstrated the physical differences arising from changes in parameter values. In either case, sufficiently accurate one-dimensional and two-dimensional active subspace approximations of the growth rate γ were acquired. A global approximation of the growth rate was also obtained for a larger range of parameter values to show that a two-dimensional active subspace representation can describe the behavior of both extreme cases near the Bi-Maxwellian state. For all distributions considered herein, these approximations yield explicit algebraic formulas for the growth rate as a function of system parameters. Lastly, we note that our methods can easily extend to analyze multispecies plasmas without a neutralizing background density, as well, wherein the active subspace method can reduce the increased complexity of the model resulting from additional parameters, e.g. masses and charges.

CRediT authorship contribution statement

Soraya Terrab: Writing – review & editing, Writing – original draft, Software, Formal analysis. **Stephen Pankavich:** Writing – review & editing, Writing – original draft, Software, Methodology, Formal analysis, Conceptualization.

Declaration of competing interest

The authors declare that they have no known competing financial interests or personal relationships that could have appeared to influence the work reported in this paper.

Data availability

Data will be made available on request.

Acknowledgments

We are grateful to the anonymous reviewer for helpful suggestions and comments that have greatly improved the paper.

Appendix A. Dimensionless model

In order to construct the dimensionless Eqs. (1), we begin with the original Vlasov–Poisson system

$$\partial_{\tilde{t}}\tilde{f} + \tilde{v}\partial_{\tilde{x}}\tilde{f} - \frac{q}{m}\tilde{E}\partial_{\tilde{v}}\tilde{f} = 0 \tag{A.1a}$$

$$\partial_{\tilde{x}}\tilde{E} = \frac{q}{m\epsilon_0}(\tilde{\rho}_0 - \tilde{\rho}(\tilde{t},\tilde{x})) \tag{A.1b}$$

$$\tilde{\rho}(\tilde{t},\tilde{x}) = m\int \tilde{f}\, d\tilde{v}. \tag{A.1c}$$

Here, $\tilde{f}(\tilde{t},\tilde{x},\tilde{v})$ represents the electron distribution, $\tilde{\rho}(\tilde{t},\tilde{x})$ is the corresponding charge density, and $\tilde{E}(\tilde{t},\tilde{x})$ is the electric field induced by the charge in the system. Additionally,

$$\tilde{\rho}_0 = \frac{1}{L_0}\int_0^{L_0} \tilde{\rho}(0,\tilde{x})\, d\tilde{x}$$

represents a background neutralizing density, and the parameters q, m, and ϵ_0 are the charge and mass of a particle and the permittivity of free space, respectively.

For each independent and dependent variable, we introduce a scaling factor:

$$\tilde{t} = T_0 t, \quad \tilde{x} = L_0 x, \quad \tilde{v} = \frac{L_0}{T_0}v$$

$$\tilde{f} = F_0 f, \quad \tilde{E} = E_0 E, \quad \tilde{\rho} = \tilde{\rho}_0\rho.$$

Rewriting (A.1) in terms of the scaled variables ultimately yields the system

$$\partial_t f + v\partial_x f - \left(\frac{qE_0T_0^2}{mL_0}\right)E\partial_v f = 0$$

$$\partial_x E = \left(\frac{qL_0\tilde{\rho}_0}{\epsilon_0 E_0}\right)(1-\rho)$$

$$\rho = \left(\frac{F_0L_0}{\tilde{\rho}_0T_0}\right)\int f(t,x,v)\, dv.$$

In order to reduce the dimension of the parameter space, we normalize the constant quantities within the parentheses. Doing so implies choosing

$$E_0 = \frac{qL_0\tilde{\rho}_0}{\epsilon_0}, \quad T_0 = \sqrt{\frac{\epsilon_0 m}{q^2\tilde{\rho}_0}}, \quad F_0 = \frac{\sqrt{\tilde{\rho}_0\epsilon_0 m}}{qL_0}. \tag{A.2}$$

With this scaling, we arrive at the dimensionless Vlasov–Poisson system, namely (1).

We assume that the background density, $\tilde{\rho}_0$, and the length scale, L_0, have been selected. The remaining parameters, E_0, T_0, and F_0, are then uniquely determined, and (1) results for any choice of $\tilde{\rho}_0$ and L_0. In particular, a standard choice is to select the length scale of the Debye length, $L_0 = \lambda_D$, where

$$\lambda_D = \sqrt{\frac{\epsilon_0 k_B T}{\tilde{\rho}_0 q^2}},$$

k_B is the Boltzmann constant and T is the temperature, and this yields the time scale of the inverse plasma frequency, namely $T_0 = \omega_p^{-1}$, where

$$\omega_p = \sqrt{\frac{q^2 \tilde{\rho}_0}{\epsilon_0 m}}.$$

These length and time scalings then imply a specific velocity scaling that can influence the value of dimensionless parameters in the distribution functions via

$$\tilde{v} = v_{\mathrm{th}} v$$

where

$$v_{\mathrm{th}} = \lambda_D \omega_p = \sqrt{\frac{k_B T}{m}}.$$

For instance, if the temperature T is increased by a certain factor $A > 0$, then the dimensionless parameter σ^2 (which is on the order of v^2) is also increased by the same factor of A.

Appendix B. Dispersion relations for Two-Stream and Bi-Maxwellian instabilities

For the steady states under consideration, explicit formulas for the growth rate within the linear regime can be computed in terms of the Z-function. In particular, assuming that the charge distribution has the form

$$f(t,x,v) = f_{eq}(v) + \delta f(t,x,v)$$

where $\delta f(t,x,v) = \alpha f_1(v)\exp(i[kx - \omega t])$, one can express the growth rate γ as a function of the frequency ω for fixed wavenumber k. The plasma dispersion relation, obtained by linearizing (1) about f_{eq} and considering plane wave solutions, is

$$\varepsilon(k,\omega) = 1 - \frac{1}{k^2}\int_{-\infty}^{\infty} \frac{f'_{eq}(v)}{v - \omega/k}\,dv. \tag{B.1}$$

Prior to computing the dispersion relation for the steady states of interest, we will perform this calculation for a Maxwellian distribution and then use this information to generalize the expression for the Two-Stream and Bi-Maxwellian cases. Thus, let us first consider a single Maxwellian equilibrium, for which the distribution of particle velocities is given by

$$f_M(v;\mu,\sigma^2) = \frac{1}{\sqrt{2\pi\sigma^2}}\exp\left(-\frac{1}{2\sigma^2}|v-\mu|^2\right).$$

Taking a derivative of this function, writing $u = \omega/k$, and substituting $z = \frac{1}{\sqrt{2\sigma^2}}(v - \mu)$ within the resulting integral of (B.1) yields

$$\varepsilon(k,ku) = 1 + \frac{1}{\sqrt{\pi}\sigma^2 k^2}\int_{-\infty}^{\infty} \frac{z}{z - \frac{1}{\sqrt{2\sigma^2}}(u-\mu)} e^{-z^2}\,dz.$$

Next, we let

$$A(u) = \frac{1}{\sqrt{2\sigma^2}}(u - \mu)$$

and rewrite the integrand as

$$\frac{z}{z - A(u)}e^{-z^2} = e^{-z^2} + \frac{A(u)}{z - A(u)}e^{-z^2}.$$

Then, the integral of the first term can be computed explicitly as $\sqrt{\pi}$, while the second involves the Z-function given by (4). Ultimately, we find

$$\varepsilon(k,ku) = 1 + \frac{1}{\sigma^2 k^2}\left[1 + A(u)Z(A(u))\right], \tag{B.2}$$

the principal root of which yields an implicit representation for computing $\gamma = \mathrm{Im}(ku)$.

For the Two-Stream function, the distribution of particle velocities is given by

$$f_{TS}(v;\mu,\sigma^2) = \frac{1}{\sqrt{2\pi\sigma^3}}|v-\mu|^2\exp\left(-\frac{1}{2\sigma^2}|v-\mu|^2\right). \tag{B.3}$$

Similar to the Maxwellian distribution, we first differentiate to find

$$f'_{eq}(v) = \frac{2}{\sqrt{2\pi\sigma^3}}(v-\mu)\exp\left(-\frac{1}{2\sigma^2}|v-\mu|^2\right) - \frac{1}{\sqrt{2\pi\sigma^5}}(v-\mu)^3\exp\left(-\frac{1}{2\sigma^2}|v-\mu|^2\right),$$

which we decompose as

$$f'_{eq}(v) = \frac{1}{\sigma^2}\left[g_1(v) - g_2(v)\right].$$

As the dispersion relation is linear in the contribution of $f'_{eq}(v)$, we use (B.1) to find

$$\varepsilon(k,\omega) = 1 - \frac{1}{\sigma^2k^2}\int_{-\infty}^{\infty}\frac{g_1(v)}{v-\omega/k}dv + \frac{1}{\sigma^2k^2}\int_{-\infty}^{\infty}\frac{g_2(v)}{v-\omega/k}dv.$$

Proceeding with the g_1 integrand and using similar substitution techniques as for the Maxwellian, including the change of variables $t = \frac{1}{\sqrt{2\sigma^2}}(v-\mu)$, we have

$$\begin{aligned}
\int_{-\infty}^{\infty}\frac{g_1(v)}{v-\frac{\omega}{k}}dv &= \frac{2}{\sqrt{2\pi\sigma^2}}\int_{-\infty}^{\infty}\frac{(v-\mu)\exp\left(-\frac{1}{2\sigma^2}|v-\mu|^2\right)}{v-\frac{\omega}{k}}dv,\\
&= \frac{2}{\sqrt{\pi}}\int_{-\infty}^{\infty}\frac{te^{-t^2}}{t-A(u)}dt,\\
&= \frac{2}{\sqrt{\pi}}\left[\int_{-\infty}^{\infty}e^{-t^2}dt + A(u)\int_{-\infty}^{\infty}\frac{e^{-t^2}}{t-A(u)}dt\right],\\
&= 2\left[1 + A(u)Z(A(u))\right],
\end{aligned}$$

where $u = \omega/k$ and $A(u) = \frac{1}{\sqrt{2\sigma^2}}(u-\mu)$. To compute the second integral, we perform the same change of variables to find

$$\begin{aligned}
\int_{-\infty}^{\infty}\frac{g_2(v)}{v-\frac{\omega}{k}}dv &= \frac{1}{\sigma^2\sqrt{2\pi\sigma^2}}\int_{-\infty}^{\infty}\frac{(v-\mu)^3\exp\left(-\frac{1}{2\sigma^2}|v-\mu|^2\right)}{v-\frac{\omega}{k}}dv,\\
&= \frac{2}{\sqrt{\pi}}\int_{-\infty}^{\infty}\frac{t^3e^{-t^2}}{t-A(u)}dt
\end{aligned}$$

where $u = \omega/k$ and $A(u) = \frac{1}{\sqrt{2\sigma^2}}(u-\mu)$. Next, we make repeated use of the identity

$$\frac{t}{t-A(u)} = 1 + \frac{A(u)}{t-A(u)}$$

in order to simplify the rational portion of the integrand, resulting in

$$\frac{t^3}{t-A(u)} = t^2 + tA(u) + A(u)^2 + \frac{A(u)^3}{t-A(u)}.$$

With this, we can perform the integration in each portion of the integral, which yields

$$\begin{aligned}
\int_{-\infty}^{\infty}\frac{g_2(v)}{v-\frac{\omega}{k}}dv &= \frac{2}{\sqrt{\pi}}\int_{-\infty}^{\infty}\left[t^2 + tA(u) + A(u)^2 + \frac{A(u)^3}{t-A(u)}\right]e^{-t^2}dt\\
&= \frac{2}{\sqrt{\pi}}\left[\int_{-\infty}^{\infty}t^2e^{-t^2}dt + A(u)\int_{-\infty}^{\infty}te^{-t^2}dt + A(u)^2\int_{-\infty}^{\infty}e^{-t^2}dt + A(u)^3\int_{-\infty}^{\infty}\frac{e^{-t^2}}{t-A(u)}dt\right]\\
&= \frac{2}{\sqrt{\pi}}\left[\frac{\sqrt{\pi}}{2} + A(u)^2\sqrt{\pi} + A(u)^3\sqrt{\pi}Z(A(u))\right]\\
&= 1 + 2A(u)^2 + 2A(u)^3Z(A(u)).
\end{aligned}$$

Reassembling the results of the g_1 and g_2 terms, we finally arrive at a simplified expression for the dispersion relation, namely

$$\varepsilon_{TS}(k,ku) = 1 - \frac{1}{\sigma^2k^2}\left[1 - 2A(u)^2 + 2\left(A(u) - A(u)^3\right)Z(A(u))\right], \tag{B.4}$$

the roots of which yield an implicit representation for $\gamma_{TS}(k,\mu,\sigma^2) = \mathrm{Im}(ku)$.

Next, we return to (B.1) and simplify the dispersion relation for the Bi-Maxwellian function, for which the distribution of particle velocities is given by

$$f_{BM}(v) = \frac{\beta}{\sqrt{2\pi\sigma_1^2}}\exp\left(-\frac{1}{2\sigma_1^2}|v-\mu_1|^2\right) + \frac{1-\beta}{\sqrt{2\pi\sigma_2^2}}\exp\left(-\frac{1}{2\sigma_2^2}|v-\mu_2|^2\right), \tag{B.5}$$

where $0 < \beta < 1$. Noting that this distribution is merely a convex combination of two Maxwellians, we use the linearity of the dispersion relation and the previously-computed formula (B.2) for each Maxwellian separately to find

$$\int_{-\infty}^{\infty} \frac{f'_{eq}(v)}{v-\omega/k}\,dv = -\frac{\beta}{\sigma_1^2}\left[1 + A_1(u)Z(A_1(u))\right] - \frac{1-\beta}{\sigma_2^2}\left[1 + A_2(u)Z(A_2(u))\right],$$

where $u = \omega/k$,

$$A_1(u) = \frac{1}{\sqrt{2\sigma_1^2}}(u-\mu_1) \qquad \text{and} \qquad A_2(u) = \frac{1}{\sqrt{2\sigma_2^2}}(u-\mu_2).$$

Thus, we have a representation for the dispersion relation as

$$\varepsilon_{BM}(k, ku) = 1 + \frac{\beta}{\sigma_1^2 k^2}\left[1 + A_1(u)Z(A_1(u))\right] + \frac{1-\beta}{\sigma_2^2 k^2}\left[1 + A_2(u)Z(A_2(u))\right],$$

and the associated growth rate $\gamma_{BM}(k, \mu_1, \mu_2, \sigma_1^2, \sigma_2^2, \beta) = \mathrm{Im}(ku)$ is computed as the principal root of $\varepsilon_{BM}(k, ku)$ given the wavenumber k.

References

[1] Landau L. Acad Sci USSR J Phys 1946;10:25–34.
[2] Ryutov DD. Plasma Phys Control Fusion 1999;41:A1–A12.
[3] Mouhot C, Villani C. Acta Math 2011;207(1):29–01.
[4] Mouhot C, Villani C. J Math Phys 2010;51:015204.
[5] Herr W. Proceedings of the CAS-CERN accelerator school: advanced accelerator physics, Trondheim, Norway, 19-29 August 2013. 2014, p. 377–403.
[6] O'Neil TM, Coroniti FV. Rev Modern Phys 1999;71(2):S404–10.
[7] Constantine P. Active subspaces: Emerging ideas for dimension reduction in parameter studies. SIAM spotlights, vol. 2, Philadelphia, PA: SIAM; 2015, p. ix+100.
[8] Saltelli A, Ratto M, Andres T, et al. Global sensitivity analysis: The primer. New York: John Wiley & Sons; 2008.
[9] Iooss B, Lemaître P. In: Dellino G, Meloni C, editors. Uncertainty management in simulation-optimization of complex systems: algorithms and applications. Boston, MA: Springer US; 2015, p. 101–22.
[10] Davidson R, Qin H. Physics of intense charged particle beams in high energy accelerators. Singapore: World Scientific; 2001.
[11] Sefkow AB, Davidson RC, Kaganovich ID, Gilson EP, Roy PK, Seidl PA, Yu SS, Welch DR, Rose DV, Barnard JJ. Nucl Instrum Methods Phys Res A 2007;577(1):289–97, Proceedings of the 16th International Symposium on Heavy Ion Inertial Fusion.
[12] Mason RJ. Phys Rev Lett 2006;96:035001.
[13] Alfvén H. Phys Rev 1939;55:425–9.
[14] Medvedev MV, Fiore M, Fonseca RA, Silva LO, Mori WB. Astrophys J 2004;618(2):L75–8.
[15] Joshi C. Phys Plasmas 2007;14(5):055501.
[16] Tokluoglu EK, Kaganovich ID, Carlsson JA, Hara K, Startsev EA. Phys Plasmas 2018;25(5):052122.
[17] Fried B, Conte S. The plasma dispersion function. London: Academic Press; 1961.
[18] Fowler TK. Phys Fluids 1964;7(2):249–56, https://aip.scitation.org/doi/abs/10.1063/1.1711192.
[19] Kaganovich ID, Sydorenko D. Phys Plasmas 2016;23(11):112116.
[20] Stix T. Waves in plasmas. College Park: American Institute of Physics; 1992.
[21] Lee FM, Shadwick BA. Phys Rev E 2023;107:L063201.
[22] van Kampen NG. Physica 1957;23:641.
[23] Case KM. Ann Physics 1959;7:349.
[24] Jackson JD. J Nucl Energy C 1960;1:171.
[25] Penrose O. Phys Fluids 1960;3(2):258–65.
[26] Sobol I, Kucherenko S. Math Comput Simulation 2009;79:3009–17.
[27] Smith R. Uncertainty quantification: Theory, implementation, and applications. Philadelphia: SIAM; 2014.
[28] Constantine P, Gleich D. 2016, arXiv:1408.0545.
[29] Grey ZJ, Constantine PG. AIAA J 2018;56(5):2003–17.
[30] Constantine PG, Doostan A. Statist Anal Data Min: ASA Data Sci J 2016;10(5):243–62.
[31] Axler S. Linear algebra done right. Springer Verlag; 1997.
[32] Pankavich S. Linear vector spaces & applications. 2020.
[33] Russi T. Uncertainty quantification with experimental data and complex system models (Ph.D. thesis), Berkeley: University of California; 2010.
[34] Constantine PG, Diaz P. Reliab Eng Syst Saf 2017;162:1–13.
[35] Constantine PG, Doostan A. Statist Anal Data Min: ASA Data Sci J 2017;10(5):243–62, https://onlinelibrary.wiley.com/doi/abs/10.1002/sam.11347.
[36] Grey ZJ, Constantine PG. AIAA J 2018;56(5):2003–17.
[37] Diaz P, Constantine P, Kalmbach K, Jones E, Pankavich S. Appl Math Comput 2018;324:141–55.
[38] Clarke C, Pankavich S. J Math Biol 2024;88:34.
[39] Pankavich S, Loudon T. Math Biosci Eng 2017;14(3):709–33.
[40] Zaghloul MR, Ali AN. ACM Trans Math Software 2012;38(2). http://dx.doi.org/10.1145/2049673.2049679.
[41] Heath R, Gamba I, Morrison P, Michler C. J Comput Phys 2012;231(4):1140–74.
[42] Terrab S, Pankavich S. sterrab/GSA_PlasmaInstabilities: Initial release. 2020.
[43] Hou YW, Chen MX, Yu MY, Wu B. J Plasma Phys 2015;81(6):905810602.
[44] Balmforth N. Commun Nonlinear Sci Numer Simul 2012;17(5):1989–97, Special Issue: Mathematical Structure of Fluids and Plasmas.